

The VMC survey – XLVI. Stellar proper motions in the centre of the Large Magellanic Cloud

Florian Niederhofer ¹★, Maria-Rosa L. Cioni ¹, Thomas Schmidt,^{1,2} Kenji Bekki,³ Richard de Grijs,^{4,5} Valentin D. Ivanov,⁶ Joana M. Oliveira ⁷, Vincenzo Ripepi ⁸, Smitha Subramanian⁹ and Jacco Th. van Loon⁷

¹Leibniz-Institut für Astrophysik Potsdam, An der Sternwarte 16, D-14482 Potsdam, Germany

²Institut für Physik und Astronomie, Universität Potsdam, Haus 28, Karl-Liebknecht-Str. 24/25, D-14476 Golm (Potsdam), Germany

³ICRAR, M468, The University of Western Australia, 35 Stirling Highway, Crawley, WA 6009, Australia

⁴School of Mathematical and Physical Sciences, Macquarie University, Balaclava Road, Sydney NSW 2109, Australia

⁵Research Centre for Astronomy, Astrophysics and Astrophotonics, Macquarie University, Balaclava Road, Sydney NSW 2109, Australia

⁶European Southern Observatory, Karl-Schwarzschild-Str. 2, D-85748 Garching bei München, Germany

⁷Lennard-Jones Laboratories, Keele University, ST5 5BG, UK

⁸INAF – Osservatorio Astronomico di Capodimonte, via Moiariello 16, I-80131 Naples, Italy

⁹Indian Institute of Astrophysics, Koramangala II Block, Bangalore 560034, India

Accepted 2022 March 8. Received 2022 February 16; in original form 2021 September 15

ABSTRACT

We present proper motion (PM) measurements within the central region of the Large Magellanic Cloud (LMC), using near-infrared data from the VISTA survey of the Magellanic Cloud system (VMC). This work encompasses 18 VMC tiles covering a total sky area of ~ 28 deg². We computed absolute stellar PMs from multiepoch observations in the K_s filter over time baselines between ~ 12 and 47 months. Our final catalogue contains $\sim 6322\,000$ likely LMC member stars with derived PMs. We employed a simple flat-rotating disc model to analyse and interpret the PM data. We found a stellar centre of rotation ($\alpha_0 = 79.95^\circ_{-0.23}^{+0.22}$, $\delta_0 = -69.31^\circ_{-0.11}^{+0.12}$) that is in agreement with that resulting from *Hubble Space Telescope* data. The inferred viewing angles of the LMC disc ($i = 33.5^\circ_{-1.3}^{+1.2}$, $\Theta = 129.8^\circ_{-1.9}^{+1.9}$) are in good agreement with values from the literature but suggest a higher inclination of the central parts of the LMC. Our data confirm a higher rotation amplitude for the young (≤ 0.5 Gyr) stars compared to the intermediate-age/old ($\gtrsim 1$ Gyr) population, which can be explained by asymmetric drift. We constructed spatially resolved velocity maps of the intermediate-age/old and young populations. Intermediate-age/old stars follow elongated orbits parallel to the bar’s major axis, providing first observational evidence for x_1 orbits within the LMC bar. In the innermost regions, the motions show more chaotic structures. Young stars show motions along a central filamentary bar structure.

Key words: surveys – proper motion – stars: kinematics and dynamics – galaxies: individual: LMC – Magellanic Clouds.

1 INTRODUCTION

The Large Magellanic Cloud (LMC) and Small Magellanic Cloud (SMC) have inspired the imagination of people for thousands of years, attempting to explain their nature. The Magellanic Clouds are visible by naked eye from the Southern hemisphere and today, we know them as a pair of interacting dwarf satellite galaxies of the Milky Way. Their close proximity (LMC ~ 50 kpc, de Grijs, Wicker & Bono 2014; SMC ~ 60 kpc, de Grijs & Bono 2015) and location below the Milky Way disc and their rich variety of stellar populations make them exceptionally interesting objects in many fields of astrophysics. In particular, the Magellanic Clouds offer us a unique opportunity to witness cosmological processes of hierarchical structure formation (galaxy interaction and minor mergers) in action.

This traditional view of the Magellanic Clouds as long-time companions to the Milky Way has changed in the last decades.

Using multiepoch *Hubble Space Telescope* (HST) observations, Kallivayalil et al. (2006a, 2013) and Kallivayalil, van der Marel & Alcock (2006b) measured proper motions (PMs) of stars in several fields across the LMC and SMC. They found that both Clouds are moving faster than previously thought. These results imply that the Magellanic Clouds are either on their first passage around the Milky Way or on a long-period orbit (see e.g. Patel, Besla & Sohn 2017). Recently, Conroy et al. (2021) reported the detection of a strong wake in the halo of the Milky Way that is caused by the gravitational interaction between the LMC and the halo of the Milky Way. The authors argue that the strength of this feature provides an independent evidence that the Magellanic Clouds are indeed on their first orbit around the Milky Way.

The Magellanic Clouds experienced several past interactions that likely caused the prominent large-scale dynamical features that we observe today. The Magellanic Stream follows the orbits of the Clouds, spanning more than 200° on the sky (see e.g. Mathewson, Cleary & Murray 1974; Nidever, Majewski & Butler Burton 2008; D’Onghia & Fox 2016). It consists of neutral and ionized gas stripped

* E-mail: fniederhofer@aip.de

both from the LMC and the SMC (e.g. Nidever et al. 2008; Richter et al. 2013; Hammer et al. 2015). Dynamical simulations suggest that a close encounter between the two Clouds ~ 2 Gyr ago led to the formation of the Magellanic Stream (see e.g. Besla et al. 2012; Diaz & Bekki 2012). The SMC is further connected to the LMC through the Magellanic Bridge (e.g. Hindman, Kerr & McGee 1963; Irwin, Kunkel & Demers 1985). This tidal feature is younger than the Magellanic Stream and formed from a direct collision of the two galaxies a few hundred Myr ago (see e.g. Diaz & Bekki 2012; Besla, Hernquist & Loeb 2013; Wang et al. 2019; Zivick et al. 2019; Schmidt et al. 2020).

Within the last years, a wealth of stellar substructures and streams within the low-surface-brightness outskirts of the Magellanic Clouds have been reported. These features attest to the perturbed nature of the periphery of the two galaxies and carry valuable information about their interaction history. Mackey et al. (2016, 2018) discovered a number of substructures to the North and South of the LMC. Later, Belokurov & Erkal (2019) identified two long and narrow arcs of stars that seemed to be pulled out of the disc of the LMC. According to their simulations, the influence of the SMC as well as that of Milky Way contributed to the formation of these tidal features. Recently, Cullinane et al. (2022) showed that a northern substructure was likely pulled out of the outer disc of the LMC, based on the dynamics and composition of the stars within that substructure. The outskirts of the SMC are distorted along its orbit around the LMC, indicating these regions have been shaped by the gravitational influence of the LMC (Belokurov et al. 2017; Mackey et al. 2018). Recently, El Youssofi et al. (2021) detected additional substructures to the East of the LMC’s disc and to the North of the SMC. Using data from the first *Gaia* data release, Belokurov et al. (2017) claimed the detection of a bridge of old RR Lyrae stars that connects the SMC with the LMC but is offset from the nominal Magellanic Bridge. The existence of this old bridge has since been questioned by Jacyszyn-Dobrzniecka et al. (2020), arguing that this feature is rather an artefact caused by the scanning law of *Gaia*. Recent studies, however, provide independent evidence that the old bridge might indeed be a real structure (El Youssofi et al. 2021; Niederhofer et al. 2021).

The LMC is classified as a barred spiral galaxy and its structure can be approximated by a flat inclined disc and a central bar. The large-scale dynamical structure of the LMC shows an ordered rotation, typical for a spiral galaxy. The rotation curve along the line-of-sight direction has been revealed for both, the gaseous component (see e.g. Luks & Rohlfs 1992; Kim et al. 1998; Olsen & Massey 2007) and stellar component (e.g. van der Marel et al. 2002; Olsen et al. 2011) of the LMC. Exploiting the full astrometric capacity of modern observing facilities, it is now possible to trace the LMC’s internal PM field as well (see e.g. van der Marel & Kallivayalil 2014; van der Marel & Sahlmann 2016; Gaia Collaboration et al. 2018; Vasiliev 2018; Wan et al. 2020; Gaia Collaboration et al. 2021a).

The mutual interactions between the Magellanic Clouds, however, have also shaped and affected the internal structure and dynamics of the LMC, thus the galaxy shows considerable discrepancies from a simple planar, rotating disc. Studies of the morphology of the disc have revealed that it is truncated towards the West (Mackey et al. 2018) and shows a warp in the south-western direction that bends up to ~ 4 kpc from the plane of the LMC in the direction of the SMC (Choi et al. 2018). Analysing the residual PM field of the LMC disc, Choi et al. (2022) constrained the impact parameter of the latest LMC–SMC encounter to be smaller than the extent of the LMC’s disc. Olsen et al. (2011) studied the line-of-sight kinematics of giant stars within the LMC. They identified a subsample of stars with a distinct kinematic signature. These stars are either rotating opposite

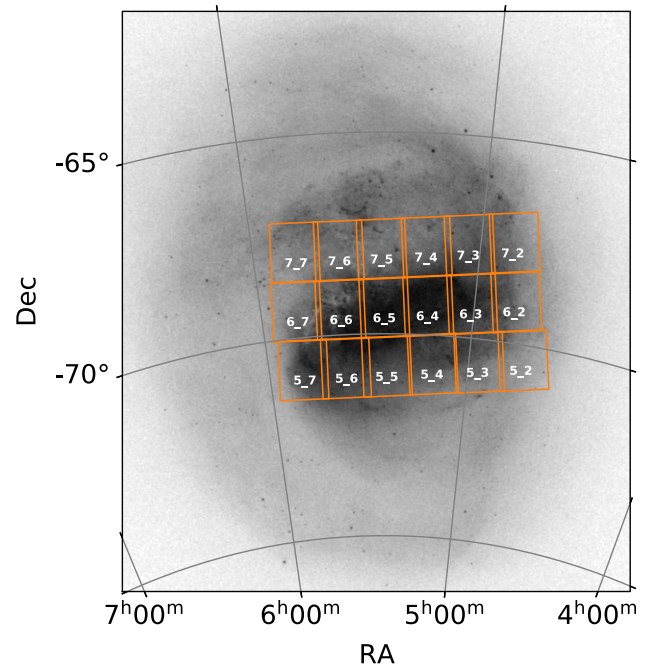


Figure 1. Positions and tile numbers of all VMC tiles, covering the central regions of the LMC. The background grey-scale image shows a stellar density map from *Gaia* eDR3.

to the LMC rotation or reside in a plane that is inclined with respect to the main LMC disc. The fact that these stars also have a lower metallicities than the average LMC disc population suggests that these outliers have once been accreted from the SMC. The bar of the LMC is displaced with respect to the disc and seems to be at a closer distance to us (Zhao & Evans 2000; Nikolaev et al. 2004). The position of the dynamical centre of the LMC is not well defined and is still a matter of debate. It has been shown that the rotational centre of the H I gas (Luks & Rohlfs 1992; Kim et al. 1998) is offset from the photometric centre (van der Marel 2001). Furthermore, the dynamic centre of the stellar component seems to be dependent on the stellar population (see Wan et al. 2020, and references therein).

In this paper, we continue our study of stellar PMs across the Magellanic system using data from the Visible and Infrared Survey Telescope for Astronomy (VISTA) survey of the Magellanic Clouds system (VMC; Cioni et al. 2011). The ability to derive median PMs of stellar populations within the Magellanic Clouds from VMC data has been demonstrated first by Cioni et al. (2014, 2016). In Niederhofer et al. (2018a), we presented an improved method to measure stellar PMs and demonstrated the potential of VMC data to measure median PMs of stellar populations that are of the same quality as those obtained by space-based missions. Subsequently, these techniques have been applied to the VMC footprint covering the SMC (Niederhofer et al. 2018b, 2021) and the Magellanic Bridge (Schmidt et al. 2020). In this study, we apply our methods to the central regions of the LMC (see Fig. 1).

The paper is organized as follows. In Section 2, we describe the observations, the photometry, and the compilation of the data catalogues. We present the calculations of the stellar PMs in Section 3. We infer the basic parameters of the LMC in Section 4 by fitting a simple model of the LMC to our kinematic data. We present the analysis of the internal motions of the central LMC in Section 5.

In Section 6, we summarize the main results of the study and offer further prospects.

2 OBSERVATIONS AND PHOTOMETRY

The VMC survey provides deep and homogeneous photometric data of the Magellanic system in the near-infrared passbands Y , J , and K_s taken with the 4.1 m VISTA telescope (Sutherland et al. 2015). The telescope is equipped with the VISTA infrared camera (VIRCAM; Dalton et al. 2006; Emerson, McPherson & Sutherland 2006) that is composed of a 4×4 array of individual detectors. To cover the LMC, a total of 68 VMC tiles are used. Each VMC tile is composed of a mosaic of six individual *pawprint* images that are taken with specific offsets in order to cover the large gaps between the 16 VIRCAM detectors and observe a contiguous area on the sky. The shifts between the individual pawprint images guarantee that most sources within a tile are observed at least twice, except for two narrow stripes at the edges of a tile. Within the LMC, the stripes of single observations overlap with adjacent tiles in East–West direction. The total sky area covered by a single tile is 1.77 deg^2 (effectively 1.50 deg^2 for the region with multiple observations). This translates into a sky area coverage of the LMC of $\sim 105 \text{ deg}^2$.

In this work, we analyse 18 VMC tiles of the central LMC region that include the bar and the base of the spiral arms (see Fig. 1). These tiles cover an area of $\sim 28 \text{ deg}^2$ and contain regions with the highest crowding within the galaxy (up to $\sim 10^6$ detected stars deg^{-2} in the VMC data). Here, point spread function (PSF) determined stellar centroids are essential for reliable PM measurements. The remaining VMC tiles covering the outer parts of the LMC with low stellar densities are analysed in a separate study (Schmidt et al. 2022). As in our previous studies, we only use observations in the K_s filter for the PM calculations (to minimize effects of differential atmospheric refraction). Each tile has at least 13 epochs of observations in the K_s passband, whereas 11 are deep exposures (375 s exposure time per pawprint image) and two are shallow exposures (187.5 s per pawprint). The observations of a single tile are distributed over a mean time baseline of 2 yr (see Table 1 for more information about the tiles analysed in this study).

For all 18 tiles studied in this work, we retrieved pawprint images at individual epochs from the VISTA Science Archive¹ (VSA; Cross et al. 2012). These images have already been reduced and calibrated by the Cambridge Astronomy Survey Unit (CASU) using version 1.5 of the VISTA Data Flow System (VDFS) pipeline (Irwin et al. 2004; González-Fernández et al. 2018, see also the CASU webpage²). We performed PSF photometry on each detector image separately, using an updated version of the photometric pipeline presented in Rubele et al. (2015). This routine is based on IRAF V2.16/DAOPHOT³ tasks (Stetson 1987; Tody 1986, 1993). In our previous studies, we found that a PSF model that is held constant per detector and is composed of an analytic function and a look-up table provides the best choice for the determination of the stellar centroids. We direct the reader to Niederhofer et al. (2021) for more details regarding the photometry on individual images.

For cross-matching, the stellar positions at individual epochs we used deep multiband tile catalogues as our master reference catalogues. These catalogues allow us to remove spurious detections from the single-epoch catalogues and, in addition, contain further information about the sources, like their colour and their morphology which are not provided in the single-epoch catalogues. The deep multiband catalogues have been created as described in Rubele et al. (2015). In short, for a given filter, all pawprint images from all epochs were first standardized to have the same reference PSF and magnitude zero-point and subsequently combined to a single deep tile image. Then, PSF photometry was performed on these tile images with the same routine as described above. The catalogues in the three filters were then combined to a single multiband catalogue using a matching radius of 1. Finally, specific offsets (that are dependent on the tile and filter) were added to the magnitudes to calibrate the photometry to the version 1.5 of the VDFS software (see González-Fernández et al. 2018).

3 PM CALCULATIONS

Our strategy to calculate the stellar PMs from VMC data is to determine them separately for each detector within each pawprint. This is to minimize any systematic effects that might arise when combining different pawprints. We broadly follow the methods presented in Cioni et al. (2016) and Niederhofer et al. (2018a, 2021) for the determination of the stellar PMs within each of the 18 LMC tiles. For this study, however, we slightly updated our techniques in an attempt to improve the quality of the PM measurements. In the following, we recapitulate the individual steps involved in the PM measurements, highlighting the changes with respect to previous works.

3.1 Coordinate transformation to common frame of reference

In a first step, we selected from the deep tile catalogues only sources that are detected in both the J and K_s filters and assigned them a unique identification number. To remove spurious detections and identify individual sources within all epochs, we cross-matched the individual-epoch catalogues with the cleaned deep catalogues using a matching radius of 0.2 arcsec (we opted to use a smaller matching radius compared to our previous studies where we used 0.5 arcsec, to minimize contributions from miss-matches). Subsequently, we extracted sources from our catalogues that are most likely background galaxies. As likely background galaxies, we selected objects in the deep multiband catalogues that satisfy the following selection criteria regarding the sources' colour, magnitude, and shape: $J - K_s > 1.0 \text{ mag}$, $K_s > 15.0 \text{ mag}$, a sharpness index in J and $K_s > 0.3$, and an associated stellar probability < 34 per cent. DAOPHOT provides a sharpness for all sources. This parameter indicates how extended a source is with respect to the model PSF. For unresolved objects, it is zero and greater than zero for extended ones. The stellar probability of a source is provided in the deep tile catalogues. It is calculated from the position in the colour–colour diagram, the local completeness and the sharpness. For more details on the adopted criteria, see Bell et al. (2019) and Niederhofer et al. (2018a, 2021).

In the next step, we transformed the detector x - and y -positions of all sources at every epoch to a common frame of reference. For each tile, we selected the epoch with the best seeing conditions as our reference epoch to which we transform all other epochs. The seeing at these epochs was between 0.75 and 0.88 arcsec. For the transformations, we used probable member stars of the LMC as our reference objects. To get a sample that is as clean as possible, we

¹<http://horus.roe.ac.uk/vsa>

²<http://casu.ast.cam.ac.uk/surveys-projects/vista/data-processing/version-1.5>

³IRAF is distributed by the National Optical Astronomy Observatory that is operated by the Association of Universities for Research in Astronomy (AURA) under a cooperative agreement with the US National Science Foundation.

Table 1. Overview of the VMC tiles used for this study. The numbers of epochs include both the deep and shallow observations (see the text).

Tile	Central coordinates		Position angle (deg)	Number of epochs	Time baseline (months)
	RA _{J2000} (h:m:s)	Dec _{J2000} (°:′:″)			
LMC 5.2	04:44:01.728	−70:22:21.000	−102.1178	13	33.5
LMC 5.3	04:56:52.488	−70:34:25.680	−99.1173	13	36.2
LMC 5.4	05:10:41.543	−70:43:05.880	−96.0612	14	33.7
LMC 5.5	05:24:30.336	−70:48:34.200	−92.6525	13	14.5
LMC 5.6	05:36:53.928	−70:49:52.320	−89.8559	13	46.8
LMC 5.7	05:49:43.944	−70:47:54.960	−86.7456	13	24.3
LMC 6.2	04:48:39.072	−68:57:56.520	−101.0355	13	33.5
LMC 6.3	05:00:42.216	−69:08:54.240	−98.2198	13	31.4
LMC 6.4	05:12:55.800	−69:16:39.360	−95.3605	13	13.0
LMC 6.5	05:25:16.272	−69:21:08.280	−92.4724	13	34.1
LMC 6.6	05:37:40.008	−69:22:18.120	−89.5708	13	12.1
LMC 6.7	05:50:03.168	−69:20:09.240	−86.6715	13	31.9
LMC 7.2	04:51:17.832	−67:31:39.000	−100.4214	13	24.3
LMC 7.3	05:02:55.200	−67:42:14.760	−97.7044	14	25.6
LMC 7.4	05:14:06.384	−67:49:21.720	−95.0871	13	24.1
LMC 7.5	05:25:58.440	−67:53:42.000	−92.3088	14	34.9
LMC 7.6	05:37:17.832	−67:54:47.880	−89.6572	13	35.0
LMC 7.7	05:48:54.000	−67:52:51.240	−86.9403	13	24.9

performed a two-step selection. In the first step, we made use of the classification presented in the *Gaia* early data release 3 (eDR3; Gaia Collaboration et al. 2021b) demonstration paper on the Magellanic Clouds (Gaia Collaboration et al. 2021a). We downloaded their base sample of *Gaia* eDR3 data from the *Gaia* data centre at the AIP⁴ and followed the procedure outlined in detail in the paper to reproduce their sample of LMC stars. Their selection is based on criteria involving the stellar magnitude, parallax, and PM. We then cross-matched this filtered sample with our deep tile VMC catalogues employing the following approach. For all VMC tiles, we used the *Gaia* PMs to first determine the sky positions of the *Gaia* stars at the mean observing epoch of that tile. We then matched the *Gaia* and VMC catalogues, selecting the nearest neighbour within a matching radius of 0.3 arcsec. This initial filter efficiently removes Milky Way foreground stars at brighter magnitudes ($K_s \lesssim 16.5$ mag). To remove any residual contamination at fainter magnitudes, especially on the red side of the LMC’s red giant branch (RGB), we applied a second selection that is based on selection boxes in the VMC K_s versus $J - K_s$ colour–magnitude diagram (CMD) (see also Kinson, Oliveira & van Loon 2021, who designed a similar procedure). The CMD regions used here were first defined by Nikolaev & Weinberg (2000) and Cioni et al. (2014) and later modified by El Yousoufi et al. (2019b, a). The left-hand panel of Fig. 2 illustrates these regions, along with their labels, on top of a stellar density (Hess) diagram in K_s versus $J - K_s$ of all sources for which PMs have been determined (see Section 3.2). In particular, we selected stars in regions A and B (young main sequence stars), G (blue supergiants), E and K (lower and upper RGB), I and N (red supergiants), J (red clump stars), and M (asymptotic giant branch stars). Our final selection yields between ~ 900 (in tile LMC 5.2 which has the lowest stellar density) and $\sim 10\,000$ (for tiles LMC 6.4 and LMC 6.5, which cover the densest regions) likely LMC member stars per detector.

To transform the detector x - and y -coordinates of the sources in the individual epochs to a reference coordinate system, we followed the steps described in Smith et al. (2018). We started by dividing each

detector into a 5×5 sub-grid and then performed the transformation on each of these sub-regions separately. This split into smaller regions is to account for any large-scale, time-dependent distortions across the detector chips. To minimize edge effects in the transformation solution, we excluded from every chip those stars in our catalogue of likely LMC nature that are located within 6 pixels from the edge of that detector. For the determination of the transformation of every subregion, we additionally included reference stars within a 20 pixel stripe of the adjacent regions. For the fitting of the transformation, we used the LEAST_SQUARES function from the PYTHON module SCIPY.⁵ We opted for a six-parameter, linear transformation that includes a shift in the x - and y -directions, a rotation, a magnification in x - and y -directions as well as a skew. The fitting was then performed in an iterative way. Within each step, we excluded sources with residuals in excess of 3σ (i.e. three times the standard deviation of the distribution of the residuals) from the best fit, until no sources were removed any more. We then applied the final transformation solution to all sources within the respective detector subregion.

We inspected the rms residuals of the fit of all detectors and epochs for every tile. The residuals were generally well below 0.07 pixels. Within seven tiles, some detector images show residuals in excess of 0.08 pixels. We found that epoch 2 of tile LMC 6.5 shows systematically higher rms residuals within all images (more than 0.03 pixels higher than the rest). We therefore decided to remove this epoch from our further analysis. In addition, we perceived that the final epoch of tile LMC 7.5 has systematically higher rms residuals that reach up to 0.12 pixels. In the case of LMC 7.5 though, removing this low-quality epoch would mean to significantly reduce the time baseline for the PM determination (from ~ 35 months to only ~ 9 months). Hence, we opted to keep this epoch for our calculations. We inspected the observing conditions of epoch 2 of tile LMC 6.5 and epoch 14 of tile LMC 7.5. We found that the reason for the lower quality of these epochs compared to the other ones is that some of the six pawprint images did not meet the required sky conditions (i.e. the FWHM was larger than required). Since the other pawprint

⁴<https://gaia.aip.de>⁵<https://www.scipy.org/>

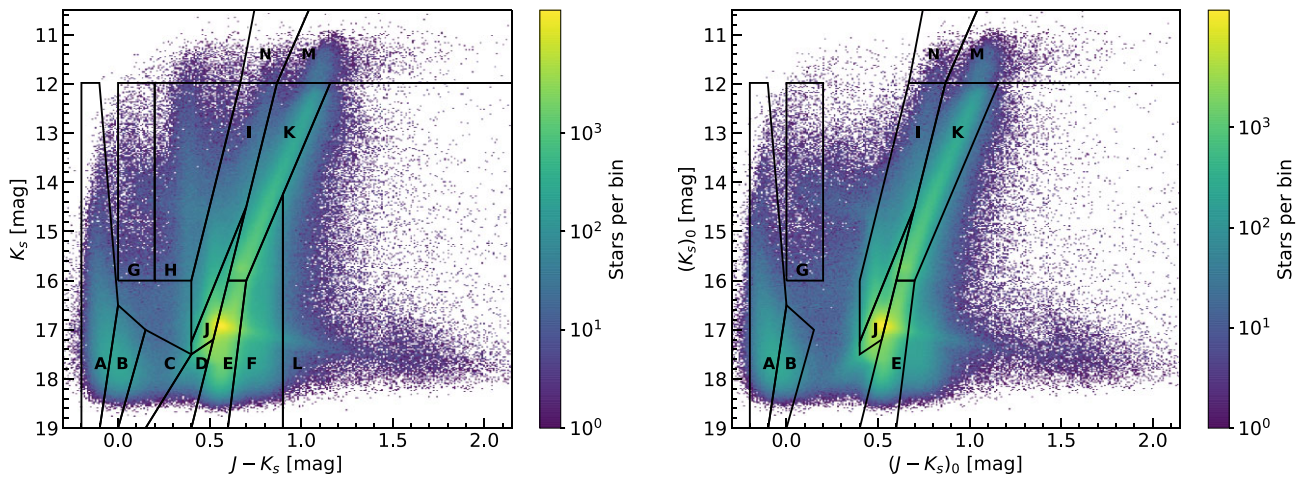


Figure 2. *Left:* K_s versus $J - K_s$ stellar density (Hess) diagram for all sources with measured PMs. The black polygons mark regions that contain different stellar populations (see the text). *Right:* As left-hand panel but with probable Milky Way stars removed and corrected for reddening. The regions marked are dominated by different LMC stellar populations.

observations of these epoch had good conditions, the overall quality of the epochs was within the requirements.

3.2 Measurement of the PMs

We calculated the PMs separately for every detector within each pawprint, using the individual catalogues containing positions in the coordinate frame of the respective reference epoch. For each source that was detected within all epochs we fitted a linear least-squares model to its coordinates as a function of the observing date. We performed the fits independently for the detector x - and y -positions. The fitting was performed employing again SCIPY’s LEAST_SQUARES function. We experimented with the various loss functions available within LEAST_SQUARES. We found that the ‘linear’ and ‘soft_l1’ loss functions provide the best results, where both functions yield virtually the same best-fitting parameters. For the sake of computation speed, we ultimately decided to use a ‘linear’ loss function.

The slopes of the fitted linear models for each source represent its relative PM, since the reference frames are constructed using likely LMC stars. Hence, in this coordinate frame, the distribution of the motion of the stars should be centred at zero. Any non-zero motion will be caused by residual motions with respect to the bulk motion of the stars (and measurement errors). We describe the calibration of the relative motions to an absolute scale in Section 3.3. We performed a zenith polynomial projection of the relative PMs to transform them from pixels day^{-1} along the detector x - and y -coordinates to angular motions along the sky RA and Dec. directions. We used the full World Coordinate System (WCS) information contained in the FITS headers of the individual detector images of the reference epochs. The projection accounts, beside the orientation of the telescope focal plane, also for the varying pixel scale across the VIRCAM detector array. The values of the PMs obtained from this projection directly correspond to the PM in RA direction, corrected for the position in Dec, $\mu_\alpha \cos(\delta)$, and the PM in Dec. direction, μ_δ . These PMs were finally converted to the commonly used unit mas yr^{-1} . Following the notation from our previous study (Niederhofer et al. 2021) and other PM studies of the Magellanic Clouds (e.g. Kallivayalil et al. 2006a; Kallivayalil et al. 2006b, 2013; van der Marel & Kallivayalil 2014; Zivick et al. 2018), we will hereafter use the following notation:

$\mu_W = -\mu_\alpha \cos(\delta)$ (the PM in the western direction) and $\mu_N = \mu_\delta$ (the PM in the northern direction).

Our final stellar PM catalogue consists of ~ 9396000 sources, of which about half are unique sources, given the overlap of individual pawprint images that form a tile. The left-hand panel of Fig. 2 illustrates these stars within a K_s versus $J - K_s$ Hess diagram.

3.3 LMC sample selection and calibration to absolute PMs

Since we did not apply any initial selection criteria to the stars in the PM catalogue, it still contains sources that are not associated with the LMC, but belong to the Milky Way foreground population. For our further analysis and the calibration of the PMs to an absolute scale, we cleaned the catalogue and sorted out those sources that are most likely not related to the LMC. We first removed those stars that were not selected as probable LMC members by Gaia Collaboration et al. (2021a). Since the VMC data are more complete than *Gaia* eDR3 in regions of high reddening (e.g. the areas East of the bar), we decided on this strategy over selecting directly likely LMC stars from the *Gaia* eDR3 catalogue. This ensures that our PM catalogue does not suffer from the same incompleteness. As described in Section 3.1, we further restricted our sample to CMD regions that are pre-dominantly populated by LMC stars (regions A, B, E, G, I, J, K, M, and N). Before the CMD-based selection, we corrected the photometry of the sources in the PM catalogue for the effect of interstellar reddening. For this, we used the reddening map from Skowron et al. (2021) that was derived from the colours of red clump stars within both Magellanic Clouds. We converted the $E(V - I)$ reddening values to extinctions in the individual VISTA passbands via the relations given in Bell et al. (2019). We note here that the reddening correction could already been applied earlier, before the selection of the reference stars for the transformation (Section 3.1). This would have resulted in a slight increase in the number of reference stars per detector. We found, however, that this does not have any significant impact on the quality of the final PM measurements.

Finally, we constrained our sample to stars with photometric uncertainties $\sigma(K_s) \leq 0.05$ mag. The final cleaned PM catalogue comprises ~ 6322000 sources, of which about half are unique sources. The right-hand panel of Fig. 2 shows the reddening-corrected K_s versus $J - K_s$ Hess diagram of the stars in the PM catalogue after the removal

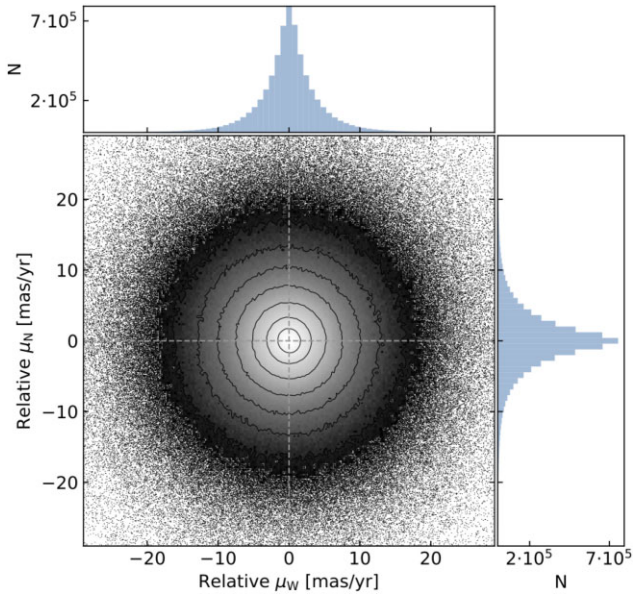


Figure 3. Vector-point diagram of relative PM in western and northern direction (μ_W and μ_N) for stars in the cleaned catalogue of likely LMC members. The histograms in the top and right-hand panel show the number distributions of the relative μ_W and μ_N .

of probable Milky Way foreground stars. The CMD regions that are used to further constrain the LMC sample are also indicated.

Note that the astrometry of VISTA pawprints shows a systematic pattern of the order of 10–20 mas resulting from residual WCS errors.⁶ This effect limits the precision of the PM measurements of single objects, however, as we have shown in previous studies (Niederhofer et al. 2018a,b, 2021), there is no noticeable systematic offset in the astrometry. The large uncertainties of the PMs of individual sources, and the resulting broad PM distribution (see Fig. 3) prevents us from cleaning our catalogue from Milky Way stars based on their VMC PMs. The PM distribution of our final sample of LMC stars has a standard deviation $\sigma \sim 5 \text{ mas yr}^{-1}$ and has an offset from zero of $-0.0028 \text{ mas yr}^{-1}$ in the West direction and $0.0064 \text{ mas yr}^{-1}$ in the North direction (about a factor of 3–4 better than the systematic offset we obtained in Niederhofer et al. 2021 for the SMC).

To calibrate the relative PMs to an absolute scale we examined different strategies. In a first attempt, we tested the method from previous VMC based PM works (Cioni et al. 2016; Niederhofer et al. 2018a,b, 2021; Schmidt et al. 2020), where absolute stellar PMs were determined with respect to background galaxies. These galaxies form a non-moving reference frame owing to their large distances and the absolute stellar motions are given by the difference between the relative motions of the stars and the reflex motions of the galaxies. We used the sample of galaxies that we identified as described in Section 3.1, applied the same transformations as to the stellar sample and measured their reflex motions in that coordinate system. We subsequently inspected the number distribution of the sample of background galaxies with measured reflex motions. Especially in regions along the LMC bar with high stellar densities, the number of background galaxies critically drops, with only ~ 10 – 20 galaxies per

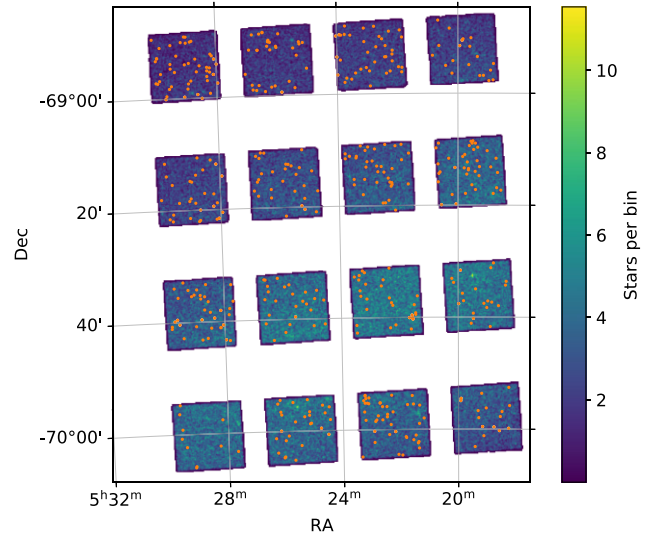


Figure 4. Single pawprint image from tile LMC 6.5. The background colour-scale indicates the density of detected sources within each detector. The orange filled circles denote sources that have been identified as background galaxies.

detector (see Fig. 4). This low number of reference objects prevents us from an accurate calibration of the relative motions to absolute values within the central bar regions of the LMC.

We therefore decided on a different strategy that involves, using *Gaia* eDR3 stars that are in common with our LMC sample for the calibration to absolute PMs. To select only high-quality *Gaia* stars, we applied the following selections: renormalized unit weight error ($\text{ruwe} \leq 1.4$) and PM uncertainties $< 0.3 \text{ mas yr}^{-1}$ in both components. For each detector within each pawprint, we determined the median difference between the VMC and *Gaia* PMs, applying an iterative 3σ clipping until convergence. The final difference gives the PM zero-point for a given detector that we subtracted from the relative VMC PM measurements to put them on an absolute scale.

3.4 Comparison with *Gaia* eDR3

To evaluate the quality and reliability of the PMs determined from the VMC data, we compared our measurements to the PMs from the *Gaia* eDR3 catalogue. Fig. 5 shows for all stars that are in common between our PM catalogue and *Gaia* eDR3 the differences in μ_W and μ_N as a function of the K_s magnitude. We only noted small offsets between the two data sets for the brightest ($K_s \lesssim 13 \text{ mag}$) stars in both PM components ($\lesssim -0.07 \text{ mas yr}^{-1}$ for μ_W and $\lesssim -0.03 \text{ mas yr}^{-1}$ for μ_N). We attribute this slight discrepancy to the small number of stars in this magnitude range. For the entire sample of stars in common, we found a median offset of $0.003 \text{ mas yr}^{-1}$ in the western direction and less than $0.001 \text{ mas yr}^{-1}$ in the northern direction, confirming an overall large-scale consistency between our derived PMs and *Gaia* eDR3.

We further examined how our results compare to the measurements from *Gaia* eDR3, as a function of the size of the stellar sample used. This will help us to assess the reliability of results that are based on variable numbers of stars. We created 500 000 sub-samples from our PM catalogue, whereas each sub-sample comprises a randomly selected number of stars (between 100 and 100 000) that was randomly drawn from the PM catalogue. For every subset, we then calculated the median difference between *Gaia* eDR3 and our

⁶See <http://casu.ast.cam.ac.uk/surveys-projects/vista/technical/astrometric-properties>

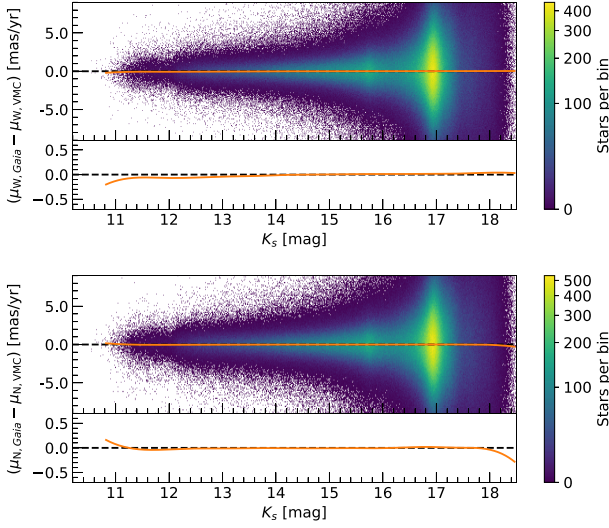


Figure 5. Difference between *Gaia* eDR3 and VMC absolute PMs of our sample of LMC stars, as a function of K_s magnitude. The orange solid line depicts the median calculated in bins of ~ 0.5 mag. The bottom plot within each of the two panels shows a zoom-in around the median to emphasize deviations from zero. *Top*: Difference in μ_W . *Bottom*: Difference in μ_N .

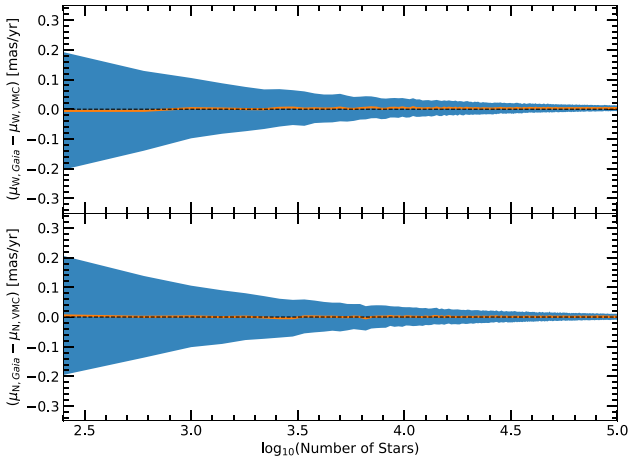


Figure 6. Median PM differences between *Gaia* eDR3 and VMC of randomly chosen subsamples (solid orange line), along with their standard deviation (blue shaded area), as a function of the sample size. *Top*: Difference in μ_W . *Bottom*: Difference in μ_N .

PM measurements. Fig. 6 shows the medians and standard deviations of these quantities in bins of 400 stars, as a function of the size of the sub-samples. We found that for sample sizes of less than 1 000 stars the 1σ scatter is above ~ 0.1 mas yr $^{-1}$, corresponding to ~ 24 km s $^{-1}$ at the distance of the LMC. The scatter decreases to ~ 0.05 mas yr $^{-1}$ (~ 12 km s $^{-1}$) for 3000 stars and is below 0.03 mas yr $^{-1}$ (~ 7 km s $^{-1}$) for samples containing more than 10 000 stars.

4 MODELLING OF THE LMC

4.1 The dynamical model

To interpret and analyse the motions within the LMC, we model the kinematics of the galaxy using our final catalogue containing absolute PMs of likely LMC members. To construct the model, we

closely follow the formalism described in detail in van der Marel et al. (2002): briefly, the LMC is described as a flat, rotating disc which is inclined with respect to the plane of the sky. The galaxy itself moves as an entity with a three-dimensional centre of mass (COM) motion and its internal velocity field is represented by circular motions within the disc. We assume here that there is no precession or nutation of the disc, since their effects are negligible within the regions studied in this work (see fig. 10 in van der Marel et al. 2002). At any given position (α, δ) , the model calculates the total resulting velocity and relates it to observable PMs in the north and west directions, by projecting the total velocity on to the plane of the sky. Hence, the resulting PM vector consists of contributions from the COM motion and from the internal velocity field at (α, δ) . The contribution of the COM motion to the observed PM field, however, is not constant across the galaxy, since differences in viewing angles result in different projections of the COM vector on to the plane of the sky (perspective expansion/contraction). The PM field resulting from the model is thus given by

$$\boldsymbol{\mu}_{\text{mod}}(\alpha, \delta) = \boldsymbol{\mu}_0(\alpha, \delta) + \boldsymbol{\mu}_{\text{int}}(\alpha, \delta), \quad (1)$$

where $\boldsymbol{\mu}_0(\alpha, \delta)$ is the projected contribution of the COM motion at (α, δ) and $\boldsymbol{\mu}_{\text{int}}(\alpha, \delta)$ is the PM resulting from the internal rotation.

The analytical model includes the following parameters:

- (i) The RA and Dec. coordinates of the dynamical centre (α_0, δ_0) .
- (ii) The COM motion along the northern and western directions $(\mu_{N,0}, \mu_{W,0})$.
- (iii) The inclination angle (i) of the LMC disc with respect to the plane of the sky.
- (iv) The position angle (Θ) of the line of nodes (the line of intersection between the plane of the LMC disc and the sky plane), measured from north to east.
- (v) The distance (D_0) to the LMC centre.
- (vi) The systemic velocity along the radial direction (v_{sys}).
- (vii) The internal rotation curve ($v_\phi(r)$).

We chose a rotation curve, $v_\phi(r)$, of the LMC disc that has the following form:

$$v_\phi(r) = v_0 \left[1 + \left(\frac{R_0}{r} \right)^\eta \right]^{-1/\eta}. \quad (2)$$

This function describes a velocity curve that first linearly rises and subsequently levels off to approach a constant terminal velocity, v_0 . The radius at which the transition takes place is given by R_0 , whereas the parameter η described the width of this transition region. Since our data probe the inner parts of the LMC disc and extends only out to radii, where the rotation curve is expected to flatten (see e.g. Wan et al. 2020; Gaia Collaboration et al. 2021a) we fixed the constant velocity v_0 in the modelling to 76 km s $^{-1}$ (e.g. van der Marel & Kallivayalil 2014; Gaia Collaboration et al. 2021a; Choi et al. 2022).

4.2 Fitting and results

For the fitting, we first spatially binned the data on a regular grid in RA and Dec. This way, we alleviate the effect of the large scatter of the individual PM measurements and further minimize the susceptibility of the final result to outliers. We created an array of 90×60 grid cells of equal area (~ 0.08 deg \times 0.08 deg) and selected only those cells that contain at least 100 stars (4940 in total). For the stars within each of these bins, we determined the median RA and Dec. coordinates (α_i, δ_i) , the median PMs in west and north directions $(\mu_{W,i}, \mu_{N,i})$, and the associated errors in the mean $(\sigma_{W,i}, \sigma_{N,i})$.

To infer the best-fitting parameters of the model and their associated uncertainties, we employed a Bayesian approach. We constructed the following log-likelihood function:

$$\ln \mathcal{L} = -0.5 \left(\sum_{i=1}^n \ln(2\pi\sigma_{W,i}^2) + \frac{(\mu_{W,i} - \mu_{W,\text{mod},i})^2}{\sigma_{W,i}^2} \right) + \ln(2\pi\sigma_{N,i}^2) + \frac{(\mu_{N,i} - \mu_{N,\text{mod},i})^2}{\sigma_{N,i}^2}. \quad (3)$$

Here, $\mu_{W,i}$, $\mu_{N,i}$, $\sigma_{W,i}$, and $\sigma_{N,i}$ are the observed quantities as defined above, whereas $\mu_{W,\text{mod},i}$ and $\mu_{N,\text{mod},i}$ denote the model PMs at the positions (α_i, δ_i) of the observed data points. The function sums over all n grid cells. We explored the posterior probability space using the Markov Chain Monte Carlo (MCMC) sampler `EMCEE` (Foreman-Mackey et al. 2013) which is a PYTHON implementation of the affine-invariant MCMC ensemble sampler (Goodman & Weare 2010). Apart from the constant rotational velocity, v_0 , we further set the distance to the LMC centre, D_0 , and the systemic line-of-sight velocity, v_{sys} , as fixed parameters. We assumed a distance of 49.9 kpc (de Grijs et al. 2014) and a radial velocity of 262.2 km s⁻¹ (van der Marel et al. 2002). The remaining parameters of the model are set as free parameters for which we chose flat priors. We ran the MCMC for 2000 steps with an ensemble of 200 walkers. After the MCMC run, we removed any stuck walkers and only considered the last 25 per cent of the chain. Fig. 7 shows the results of the MCMC run in the form of a corner plot (Foreman-Mackey 2016). Note that, for simplicity, we calculated the position angle of the line of nodes in the model from west to north. This angle is denoted θ in the corner plot. The actual position angle, measured from north to east, is then simply given by $\Theta = \theta - 90^\circ$. We found for the best-fitting parameters:

$$\begin{aligned} \alpha_0 &= 79.95^\circ_{-0.23}^{+0.22}, & \delta_0 &= -69.31^\circ_{-0.11}^{+0.12} \\ \mu_{W,0} &= -1.867_{-0.008}^{+0.008} \text{ mas yr}^{-1}, & \mu_{N,0} &= 0.314_{-0.014}^{+0.014} \text{ mas yr}^{-1} \\ i &= 33.5^\circ_{-1.3}^{+1.2}, & \Theta &= 129.8^\circ_{-1.9}^{+1.9} \\ R_0 &= 2.64_{-0.10}^{+0.09} \text{ kpc}, & \eta &= 3.2_{-0.4}^{+0.5} \end{aligned}$$

The quoted values and the corresponding uncertainties result from the 50th, 16th, and 84th percentiles of the final marginalized distributions.

We also examined how sensitive our results are to the assumed value of v_0 . Recently, Wan et al. (2020) combined *Gaia* DR2 PMs with photometry from SkyMapper (Wolf et al. 2018) to study the kinematics of carbon stars, RGB stars, and young stars within the LMC. For their sample of carbon stars they found a value of $v_0 = 83.6$ km s⁻¹. We re-ran the MCMC, now fixing v_0 to the value from Wan et al. (2020). As expected, we obtained different values for parameters of the rotation curve, in particular, we got a slightly larger value for the turnover radius ($R_0 = 2.81 \pm 0.11$ kpc) and a smaller value for η (2.5 ± 0.3). The results we obtained for the centre coordinates, the PMs, and the orientation, however, were within the 1σ uncertainties from our initial run, indicating that our results are largely insensitive to the exact choice of v_0 .

From the results of the MCMC, we noted a strong correlation between the inferred COM motion and the dynamical centre coordinates (see Fig. 7). The main reason for this is that we here cover only the inner parts of the LMC where the rotation curve is mostly linearly rising. In such linear PM field, the position of the rotational centre is degenerate with the COM motion. Given this degeneracy, we also investigated the case where we fixed the position of the dynamical centre. We set the coordinates to $(\alpha_0 = 81.07^\circ, \delta_0 = -69.41^\circ)$, as derived from *Gaia* eDR3 PMs (Gaia Collaboration et al. 2021a).

For this case, we further assumed a simplified rotation curve that only consists of the linear part, i.e. $v_\phi(r) = \omega r$ with constant angular velocity ω . Employing the same MCMC analysis as before, we found the following best-fitting model parameters (see also Fig. 8):

$$\begin{aligned} \mu_{W,0} &= -1.862_{-0.002}^{+0.002} \text{ mas yr}^{-1}, & \mu_{N,0} &= 0.383_{-0.002}^{+0.002} \text{ mas yr}^{-1} \\ i &= 28.7^\circ_{-1.5}^{+1.4}, & \Theta &= 126.0^\circ_{-2.6}^{+2.5} \\ \omega &= 24.22_{-0.30}^{+0.29} \text{ km s}^{-1} \text{ kpc}^{-1}. \end{aligned}$$

With the dynamical centre held fixed at the position as determined by Gaia Collaboration et al. (2021a), we found that the motion in northern direction increased, from 0.314 mas yr⁻¹ to 0.383 mas yr⁻¹, whereas the motion in western direction remained within the uncertainties. This behaviour is expected from the correlation between α_0 and $\mu_{N,0}$ and the difference between the two centres that is primarily along the RA direction. Further, the inferred inclination and position angles decreases from 33.5° to 28.7° and from 129.8° to 126.0°, though, the values of the latter remain within the uncertainties.

4.3 Comparison with previous estimates from the literature

To put our inferred best-fitting parameters of the LMC from our two approaches into context, we compare them to results from the literature (see Table 2). The location of the LMC's centre is a quantity that has been debated in the literature for many years without a conclusive answer. Different tracers that have been used to determine the centre have led to different results, reflecting the disturbed nature of the LMC. Fig. 9 illustrates various centre positions presented by literature studies together with the one determined in this work. Luks & Rohlfs (1992) and, later, Kim et al. (1998) measured the rotational centre of the gaseous H I disc. The two studies found $(\alpha_0 = 78.13^\circ, \delta_0 = -69.00^\circ)$ and $(\alpha_0 = 79.40^\circ, \delta_0 = -69.03^\circ)$, respectively (note that the coordinates from Luks & Rohlfs 1992 as stated here have been precessed to the ICRS). These centres are located on the western side of the bar and are shifted with respect to the photometric bar centre which van der Marel (2001) found to be at $(\alpha_0 = 81.28^\circ, \delta_0 = -69.78^\circ)$. From the radial velocities of carbon stars within the LMC, van der Marel et al. (2002) deduced a dynamical centre at $(\alpha_0 = 81.91^\circ, \delta_0 = -69.87^\circ)$, which, they said, is in agreement with the photometric centre of the LMC bar but inconsistent with the H I centre. van der Marel & Kallivayalil (2014) studied in detail the velocity structure of the LMC, employing the PM data set that was presented in Kallivayalil et al. (2013) and obtained using three epochs of *HST* observations. They found for the PM dynamical centre $(\alpha_0 = 78.76^\circ, \delta_0 = -69.19^\circ)$, which is in accordance with the H I centre. Combining the PM data with line-of-sight velocity measurements of samples of old and young stars, van der Marel & Kallivayalil (2014) found for the central coordinates $(\alpha_0 = 79.88^\circ, \delta_0 = -69.59^\circ)$ and $(\alpha_0 = 80.05^\circ, \delta_0 = -69.30^\circ)$, respectively. Wan et al. (2020) studied the dynamics of different stellar populations within the LMC. For the carbon star population the authors found $(\alpha_0 = 80.90^\circ, \delta_0 = -68.74^\circ)$. This position is close to their derived centre of RGB stars $(\alpha_0 = 81.23^\circ, \delta_0 = -69.00^\circ)$, but inconsistent with the radial velocity centre of carbon stars as determined by van der Marel et al. (2002). We note here that the way the sources are selected, even for the same type of tracer, may result in a different location of the centre. van der Marel et al. (2002) selected a sample of spectroscopically confirmed carbon stars that are located at larger radii from the LMC centre. Wan et al. (2020) identified carbon stars through their position in the SkyMapper CMD. Their sample is distributed over a large area of the LMC, covering also the inner regions. The centre Wan et al. (2020) found for the young stars

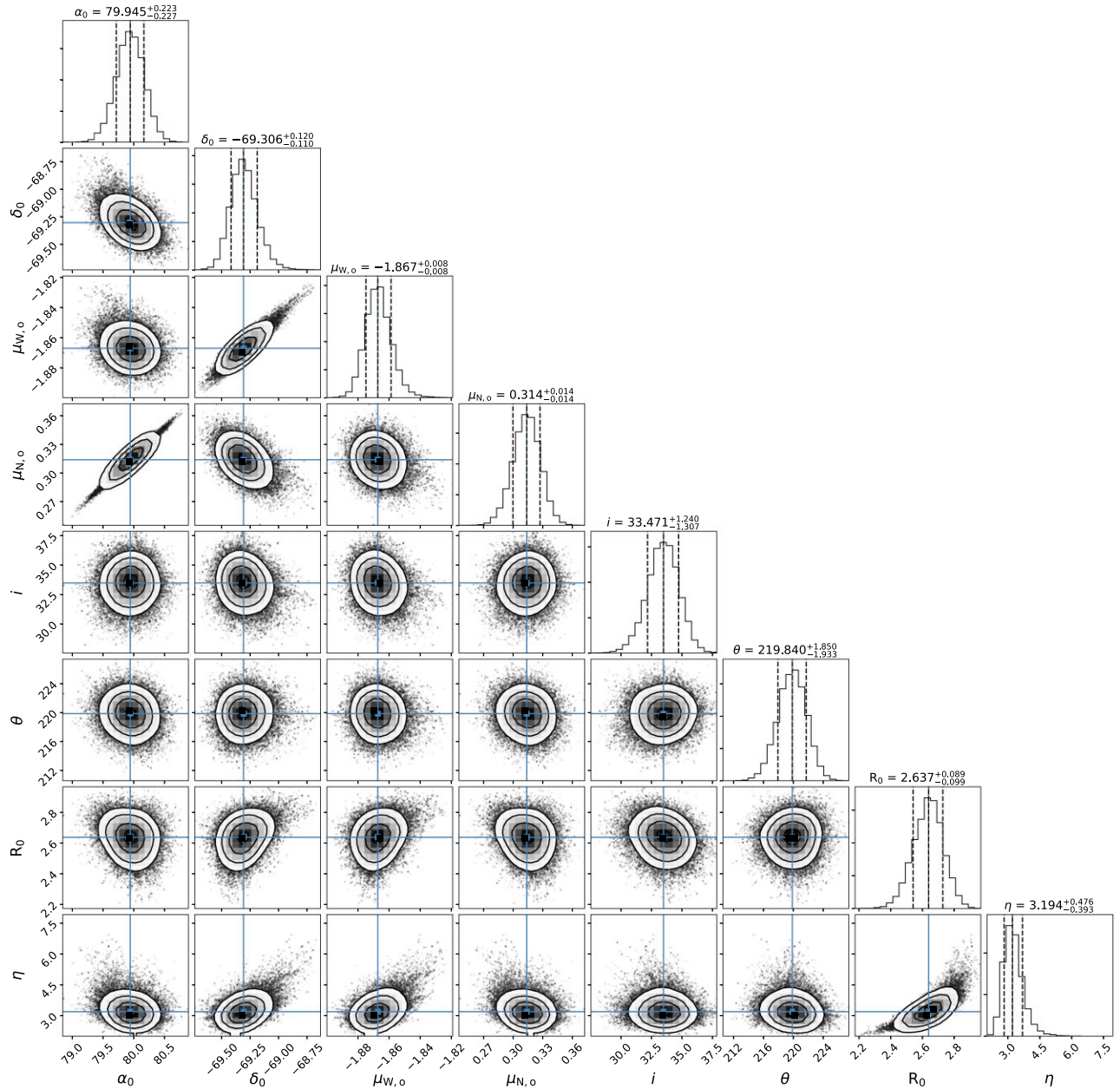


Figure 7. Corner plot showing the results of the MCMC sampling for the LMC model fit to the PM data. The scatter plots illustrate the two-dimensional marginalized posterior probability distributions of pairwise model parameters. The histograms show the projected distributions in one dimension for all parameters. The blue solid lines mark the position of the 50th percentile in each plot, whereas the black dashed lines indicate the 16th and 84th percentile. The panels show from top to bottom and left to right: The RA coordinate of the dynamical centre (α_0), the Dec. coordinate of the dynamical centre (δ_0), the COM motion in west direction ($\mu_{W,0}$), the COM motion in north direction ($\mu_{N,0}$), the inclination of the LMC disc (i), the position angle of the line of nodes (θ), measured from west to north, the scale radius of the rotation curve (R_0), and the exponential coefficient of the rotation curve (η).

($\alpha_0 = 80.98^\circ$, $\delta_0 = -69.69^\circ$), however, is displaced with respect to centres of the two older populations and is close to the photometric centre of the bar. Gaia Collaboration et al. (2021a) determined the centre of the PM rotation to be at ($\alpha_0 = 81.07^\circ$, $\delta_0 = -69.41^\circ$), which falls between the PM centres of the old populations as derived by Wan et al. (2020), on the one hand, and the photometric centre on the other hand. Recently, Choi et al. (2022) studied the PM field of evolved stars within the LMC disc. They combined PM data from *Gaia* eDR3 with radial velocity measurements of RGB, asymptotic giant branch (AGB) and red supergiant stars and fitted a model to the three-

dimensional kinematics of the stars. As the dynamical centre of the LMC, they adopted the centre inferred from the young red supergiant stars, which was found to be at ($\alpha_0 = 80.443^\circ$, $\delta_0 = -69.272^\circ$). When leaving the dynamical centre as a free parameter in our model, we inferred the position of the centre to be at ($\alpha_0 = 79.95^\circ_{-0.23}$, $\delta_0 = -69.31^\circ_{-0.11}$). This is consistent within the errors with the centres derived from *HST* data when combined with radial velocities. We note that our result is further in close agreement with the positions of two additional objects: the spiral-shaped H II region LHA 120-N 119 which has been considered to reside at the centre of the LMC,

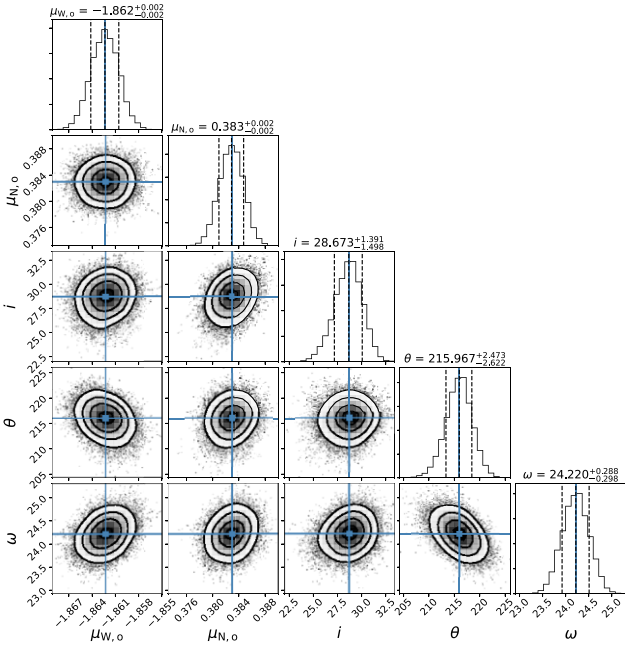


Figure 8. As Fig. 7 but now for fixed coordinates of the dynamical centre (α_0, δ_0). Here, the panels show from top to bottom and from left to right: The COM motion in west direction ($\mu_{W,0}$), the COM motion in north direction ($\mu_{N,0}$), the inclination of the LMC disc (i), the position angle of the line of nodes (θ), measured from west to north and the angular velocity (ω).

given its position and morphology (see e.g. Pennock et al. 2021) and the position of a tentative central black hole in the LMC. Based on MUSE data, Boyce et al. (2017) analysed the kinematics of the central square degree of the LMC. They found a 3σ upper limit of $10^7 M_\odot$ for a putative central black hole. However, the position they provide is only at the 1σ confidence level.

Our values for the COM motion of the LMC are in general agreement with the range of measurements from other studies. In particular, $\mu_{W,0}$ and $\mu_{N,0}$ agree best with the values found by Wan et al. (2020), Gaia Collaboration et al. (2021a), and Choi et al. (2022). We further note that our results for $\mu_{N,0}$ are significantly larger than what was found by van der Marel & Kallivayalil (2014), using PMs from *HST* observations and by Gaia Collaboration et al. (2018) using *Gaia* DR2 PMs.

The viewing angles under which we see the LMC have been estimated using various tracers and techniques. Like for the centre location, results from different studies cover a wide range of values, suggesting that the various stellar populations and the structures they trace within the galaxy do not reside in the same plane but are warped and tilted with respect to each other. Thus, the results obtained depend on the studied region and sky coverage, as well as on the stellar tracer used. The orientation can be estimated using stellar dynamics (as it has been done in this study) or using a pure geometrical approach. Such geometric determinations employ distance indicators like Cepheid stars or red clump stars to fit a flat plane to the three-dimensional distribution of these stars. We found for the area studied in this work (the central $\sim 7 \times 4$ degrees of the LMC) an inclination of $i = 33.5^\circ \pm_{-1.3}^{+1.2}$ and a position angle of $\Theta = 129.8^\circ \pm_{-1.9}^{+1.9}$ (dynamical centre as a free parameter) and an inclination of $i = 28.7^\circ \pm_{-1.5}^{+1.4}$ and a position angle of $\Theta = 126.0^\circ \pm_{-2.6}^{+2.5}$ (fixing the centre position). Our values for the inclination are in general agreement with the measurements from other studies, whereas our results of the position angle are lower than what was found in most studies. Based on

Cepheid distances within the central ~ 4 deg of the LMC, Nikolaev et al. (2004) found an inclination of $30.7^\circ \pm 1.1^\circ$ which is close to what we found for the inclination for a similar portion of the LMC. Interestingly, for the case where we left the centre as a free parameter, our derived viewing angles are also consistent with what was found by van der Marel et al. (2002) and Gaia Collaboration et al. (2021a), although the values from these two studies were obtained from more extended portions of the galaxy. Inno et al. (2016) (using Cepheids), Subramanian & Subramanian (2013), and Choi et al. (2018) (both using red clump stars) analysed the geometry and structural parameters of the LMC disc. For their studied areas, they found consistent values for the inclination of $\sim 25^\circ$ (Inno et al. 2016: $25.05^\circ \pm 0.55^\circ$; Subramanian & Subramanian 2013: $25.7^\circ \pm 1.6^\circ$; Choi et al. 2018: $25.86^\circ \pm_{-1.39}^{+0.73}$). These three studies and also Choi et al. (2022) further investigated the variation of the viewing angles as a function of the galactocentric distance and all found variations of i and Θ within the inner $\sim 3^\circ$ with respect to the outer regions, indicating that the bar is orientated differently than the disc of the LMC. Whereas Inno et al. (2016) and Choi et al. (2018, 2022) found that the inclination and position angle both increase with decreasing radius, Subramanian & Subramanian (2013) found a smaller inclination and a larger position angle in the inner regions. Our inferred values for the inclination angle would thus support the scenario of the bar being more inclined than the disc. However, our derived low values of the line-of-nodes position angle are not in agreement with an increased position angle of the bar.

5 INTERNAL MOTIONS OF THE LMC

With the help of the basic parameters of the LMC galaxy that we determined in the previous section, we are now able to analyse the internal velocity field in the frame of the LMC (i.e. in a frame where the LMC is at rest, that is aligned with the plane of the galaxy and where the motions are corrected for perspective contraction). We de-projected the measured PMs back to the plane of the LMC by solving equations (5), (9), (11), and (13) in van der Marel et al. (2002) for v'_x and v'_y , the velocities within the LMC disc plane. Note that this de-projection is uniquely defined without the knowledge of the individual radial velocities of the stars, since we assume that the motions are solely within the disc (without any motion perpendicular to the plane of the disc). The de-projection and determination of v'_x and v'_y was done using the parameters resulting from our model with a free dynamical centre ($\alpha_0 = 79.95^\circ$, $\delta_0 = -69.31^\circ$, $\mu_{W,0} = -1.867 \text{ mas yr}^{-1}$, $\mu_{N,0} = 0.314 \text{ mas yr}^{-1}$, $i = 33.5^\circ$, and $\Theta = 129.8^\circ$).

5.1 Rotation curves

We determined the median tangential velocity v_ϕ within 15 radial bins of ~ 0.27 kpc to construct the rotation curve of the inner parts of the LMC. The result is illustrated in Fig. 10 as green data points. In the figure, we also show as a green solid line the theoretical rotation curve (equation 2) that follows from our inferred best-fitted model parameters. As can be seen, the measured rotation velocities are well reproduced by the model curve. From the figure, it is also evident that our data trace the linear portion of the rotation curve and the transition region but do not reach the parts where the rotation approaches the constant terminal velocity v_0 . From our model, we found for the transition radius R_0 a value of 2.64 ± 0.09 kpc which is within the range of measurements from other works. It is closest to the measurement from Gaia Collaboration et al. (2021a) who employed the same form of the parametrized velocity curve for the fitting as we did in this study. They found $R_0 = 2.94$ kpc for a dynamical centre

Table 2. Collection of derived parameters of the LMC disc from this work and from literature studies.

α_0 (deg)	δ_0 (deg)	$\mu_{W,0}$ (mas yr ⁻¹)	$\mu_{N,0}$ (mas yr ⁻¹)	i (deg)	Θ (deg)	Reference
$79.95^{+0.22}_{-0.23}$	$-69.31^{+0.12}_{-0.11}$	$-1.867^{+0.008}_{-0.008}$	$0.314^{+0.014}_{-0.014}$	$33.5^{+1.2}_{-1.3}$	$129.8^{+1.9}_{-1.9}$	This work (free centre)
81.07^a	-69.41^a	$-1.862^{+0.002}_{-0.002}$	$0.383^{+0.002}_{-0.002}$	$28.7^{+1.4}_{-1.5}$	$126.0^{+2.5}_{-2.6}$	This work (fixed centre)
81.91 ± 0.98	-69.87 ± 0.41	–	–	34.7 ± 6.2	129.9 ± 6.0	van der Marel et al. (2002)
79.40^b	-69.03^b	–	–	30.7 ± 1.1	151.0 ± 2.4	Nikolaev et al. (2004)
81.91 ± 0.98^c	-69.87 ± 0.41^c	–	–	–	142 ± 5	Olsen et al. (2011)
79.91^d	-69.45^d	–	–	25.7 ± 1.6	141.5 ± 4.5	Subramanian & Subramaniam (2013)
78.76 ± 0.52	-69.19 ± 0.25	-1.910 ± 0.020	0.229 ± 0.047	39.6 ± 4.5	147.4 ± 10.0	van der Marel & Kallivayalil (2014) (PMs)
79.88 ± 0.83	-69.59 ± 0.25	-1.895 ± 0.024	0.287 ± 0.054	34.0 ± 7.0	139.1 ± 4.1	van der Marel & Kallivayalil (2014) (PMs + v_{LOS} old stars)
80.05 ± 0.34	-69.30 ± 0.12	-1.891 ± 0.018	0.328 ± 0.025	26.2 ± 5.9	154.5 ± 2.1	van der Marel & Kallivayalil (2014) (PMs + v_{LOS} young stars)
80.78^e	-69.30^e	–	–	25.05 ± 0.55	150.76 ± 0.07	Inno et al. (2016)
82.25^f	-69.5^f	–	–	$25.86^{+0.73}_{-1.39}$	$149.23^{+6.43}_{-8.35}$	Choi et al. (2018)
78.77^g	-69.01^g	-1.850 ± 0.030	0.234 ± 0.030	[30.0,40.0]	[111.4, 134.6]	Gaia Collaboration et al. (2018)
80.90 ± 0.29	-68.74 ± 0.12	-1.878 ± 0.007	0.293 ± 0.018	25.6 ± 1.1	135.6 ± 3.3	Wan et al. (2020) (Carbon Stars)
81.23 ± 0.04	-69.00 ± 0.02	-1.824 ± 0.001	0.355 ± 0.002	26.1 ± 0.1	134.1 ± 0.4	Wan et al. (2020) (RGB Stars)
80.98 ± 0.07	-69.69 ± 0.02	-1.860 ± 0.002	0.359 ± 0.004	29.4 ± 0.4	152.0 ± 1.0	Wan et al. (2020) (Young Stars)
80.61^h	-69.58^h	–	–	22 ± 4	167 ± 7	Cusano et al. (2021)
81.07	-69.41	-1.847	0.371	33.28	130.97	Gaia Collaboration et al. (2021a) (free centre)
81.28^i	-69.78^i	-1.858	0.385	34.08	129.92	Gaia Collaboration et al. (2021a) (fixed centre)
80.443	-69.272	1.859	0.375	$23.396^{+0.493}_{-0.501}$	$138.856^{+1.360}_{-1.370}$	Choi et al. (2022)

^aPM centre taken from Gaia Collaboration et al. (2021a); ^bH I rotational centre taken from Kim et al. (1998); ^crotation centre from carbon stars radial velocities, taken from van der Marel et al. (2002); ^dphotometric centre from de Vaucouleurs & Freeman (1972); ^ecentre of the Cepheid distribution; ^fcentre of the outer isophlets taken from van der Marel (2001); ^gH I rotational centre taken from Luks & Rohlfs (1992); ^hcentre of the RR Lyrae distribution; ⁱphotometric centre taken from van der Marel (2001).

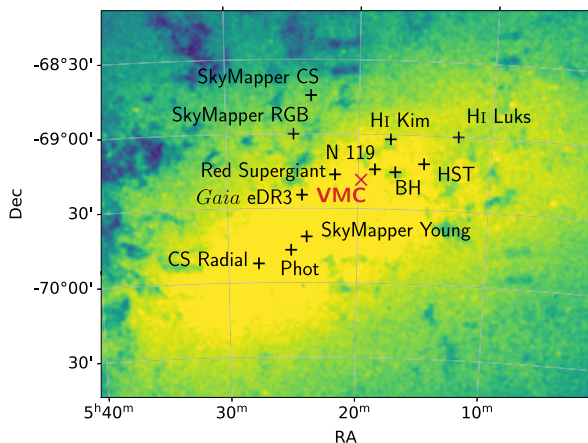


Figure 9. Illustration of various inferred positions of the LMC’s centre, from this study (denoted as VMC) and from the literature. The background colour image displays the density of stars with measured VMC PMs. The other labels in the figure refer to the following centre estimates: H I Luks and H I Kim: H I rotation curve from Luks & Rohlfs (1992) and Kim et al. (1998), respectively; HST: HST PMs from van der Marel & Kallivayalil (2014); Phot: photometric centre from van der Marel (2001); CS Radial: carbon stars radial velocities from van der Marel et al. (2002); Gaia eDR3: PMs from Gaia eDR3 from Gaia Collaboration et al. (2021a); SkyMapper CS, RGB and Young: SkyMapper photometry combined with Gaia DR2 PMs of carbon, RGB and young stars from Wan et al. (2020); Red Supergiant: Gaia eDR3 PMs combined with line-of-sight velocities of red supergiants (Choi et al. 2022). We also show here the position of a possible central black hole (BH) as inferred by Boyce et al. (2017), as well as the position of the spiral-shaped H II region LHA 120-N 119 (N 119).

fixed at the photometric centre and $R_0 = 2.89$ kpc when leaving the centre coordinates as a free parameter. Other PM studies of the LMC found for the radius, after which the rotation curve becomes flat, values of 1.18 ± 0.48 kpc (van der Marel & Kallivayalil 2014) and

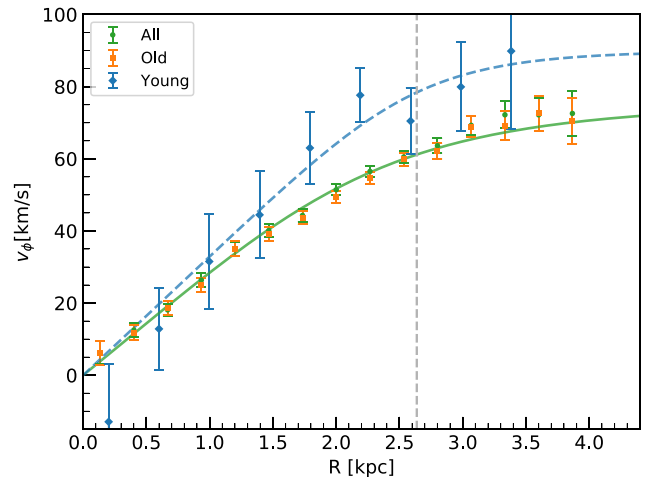


Figure 10. Measured rotation curves resulting from the PMs of all stars (green dots) of only old stars (orange squares) and of only young stars (blue diamonds). The green solid line indicates the rotation curve, resulting from our best-fitting model parameters. The blue dashed line shows a rotation curve that was fitted to the young population only. The vertical grey dashed line marks the inferred transition radius R_0 from the entire stellar sample.

3.39 ± 0.12 kpc (Wan et al. 2020). Both studies assumed a simplified rotation curve that only consists of a linearly rising and a flat part.

We further examined the rotation curve for the young ($\lesssim 0.5$ Gyr) and intermediate-age/old ($\gtrsim 1$ Gyr) stellar populations separately. For the sample of young stars, we selected in the K_s versus $J - K_s$ CMD the young main-sequence stars (regions A and B), supergiants (region G), and red supergiants (region N). We did not include region I (supergiants), since even after the correction for reddening, this CMD region still contains a non-negligible fraction of stars from the RGB. For the intermediate-age/old stellar sample, we chose RGB stars (regions E and K), AGB stars (region M), and red clump stars (region J). The orange squares in Fig. 10 illustrate v_ϕ as a function of

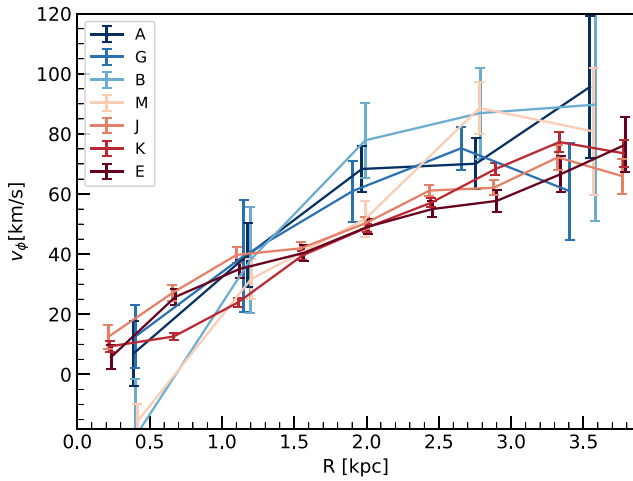


Figure 11. Measured rotation curves for the individual stellar populations that have been selected based on the CMD regions (see the text). The rotation curves have been constructed using bin sizes of 0.8 kpc for regions A, G, B, and M and 0.4 kpc for regions J, K, and E. In the figure, we did not include regions I (mixture of young supergiant and RGB stars) and N (not enough stars to construct the rotation curve).

R for the intermediate-age/old stellar populations. These data points closely follow the relation of the entire stellar sample, indicating that it is dominated by the older population. For the construction of the rotation curve of the young population, we chose a larger bin size (0.4 kpc) owing to the low number of young stars. The resulting curve is displayed as blue diamonds in Fig. 10. From a comparison of the data points from the young and intermediate-age/old populations, it is evident that the young stars follow a different rotation curve than the older population. We fitted a model curve of the form of equation (2) to the data points of the young population (blue dashed line in Fig. 10). The best-fitting solution implies that the young stars, compared to the older stars, follow a curve that has a steeper linear part as well as a higher constant velocity, at least within the inner parts. This behaviour is expected and is in agreement with PMs from *Gaia* eDR3 (Gaia Collaboration et al. 2021a) and also line-of-sight velocity measurements. van der Marel & Kallivayalil (2014) found that young red supergiant stars have a higher rotational velocity than older red giant and AGB stars. They measured $v_{0, \text{LOS}} = 55.2 \pm 10.3 \text{ km s}^{-1}$ for their old stellar sample and $v_{0, \text{LOS}} = 89.3 \pm 18.8 \text{ km s}^{-1}$ for the young stars. From the fit to our sample of young stars, we obtained a rotation amplitude of $v_0 = 90.1 \pm 9.0 \text{ km s}^{-1}$ which is consistent with the results by van der Marel & Kallivayalil (2014). The higher rotation speed of the younger stellar population, compared to the older population, can be explained by an asymmetric drift, where the smaller velocity dispersion of the young population leads to higher rotation velocity (see van der Marel, Kallivayalil & Besla 2009; van der Marel & Kallivayalil 2014).

Looking at the separate rotation curves of the individual stellar populations (see Fig. 11), we can see that the different young populations (within CMD regions A, B, and G) all show steeper rotation curves than the ones from the intermediate-age/old populations (within CMD regions J, K, and E). Their curves cross at a radius of ~ 1 kpc. The intermediate-age/old populations show similar curves, whereas there seem to be moderate differences within the inner ~ 1.5 kpc between the red clump (region J) and lower RGB (region E) population on the one side, and the upper RGB (region K) population on the other side. Within this spatial region, the tangential velocity

of the upper RGB stars falls below the rotation curve resulting from the best-fitting model. The lower mean velocity could be explained by an overall older population of upper RGB stars within the central bar region. An interesting case depicts the rotation curve of the AGB stars (region M). The innermost parts show indications of a negative tangential velocity. Between radii of ~ 1 and ~ 2 kpc, the rotation curve follows the ones from the RGB and red clump stars. At ~ 2 kpc, a jump in v_ϕ to higher values is evident, after which the rotation velocity of the AGB stars is more similar to the one of the young stars. This peculiarity can also be seen in the tangential velocity curves presented in Gaia Collaboration et al. (2021a). Since our sample of AGB stars covers a broad range of ages (between ~ 1 Gyr and ~ 5 Gyr; see El Youssoufi et al. 2019b), we speculate that this jump is caused by a transition between different morphological features that trace stars with different median ages. Within ~ 2 kpc, the AGB stars are distributed within the bar, whereas at radii larger than ~ 2 kpc, the AGB stars are situated within a spiral arm that contains stars that are on average younger than the bar population.

While examining the rotation curve of the combined young stellar populations shown in Fig. 10, we also noted that the innermost radial bin of the young stellar population shows a negative median tangential velocity. Together with the rotation curve of the AGB stars, this might hint at a population of stars in the very central parts of the LMC that rotates slower than expected or even moves in a direction opposite the main sense of rotation of the galaxy. An alternative explanation is that the negative tangential velocities of the young stars are caused by motions within a disc that is tilted and displaced with respect to that defined by the intermediate-age/old stellar population. This interpretation is supported by the fact that the dynamical centre and disc geometry of the LMC found in previous literature studies depend on the stellar tracers used. To further assess, this we fitted our dynamical model to our young stellar sample only to infer their structural parameters. However, we found that the data of solely the young stellar population did not provide sufficient quality for the fitting and the MCMC did not converge. We therefore decided to use literature measurements to de-project the PMs of the young stars. We found that employing the parameters from Wan et al. (2020) for young main-sequence stars and from Choi et al. (2022) for young red supergiants leads to tangential velocities within the innermost regions that are consistent with positive values. Gaia Collaboration et al. (2021a) also reported the discovery of regions of low and negative rotational velocities within the central LMC regions. They argue that such signatures could either be caused by counter-rotating stars or deviations from a simple planar velocity field.

We finally compare our rotation curve with the results obtained by Schmidt et al. (2022) who studied the PMs of stars within the outer VMC tiles of the LMC, using a combination of VMC and *Gaia* eDR3 data. The tangential velocities from their study are illustrated in Fig. 12, along with the best-fitting rotation curves of the combined and young stellar population from this work, for comparison (as displayed in Fig. 10). Also shown is the rotation curve of the combined stellar populations from Gaia Collaboration et al. (2021a). The small data points indicate the median tangential velocities within individual Voronoi cells. We can see that most of the Voronoi cells show velocities that lie above the rotation curves resulting from this work and from *Gaia* eDR3. There are, however, also a number of cells with velocities that are considerably smaller. These data points belong to regions in the south-eastern part of the LMC disc that shows a systematically slower rotation. Schmidt et al. (2022) relate this peculiar kinematic behaviour to a population of stripped SMC stars that rotates in the opposite sense and therefore dilutes the rotational signal in these parts of the LMC disc. We further

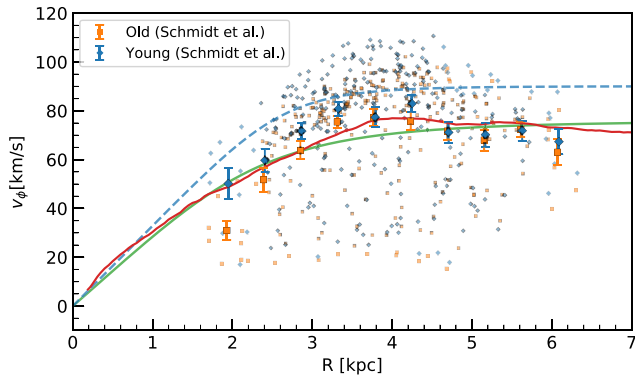


Figure 12. Measured rotation velocities of the outer VMC tiles of the LMC from Schmidt et al. (2022). The small coloured data points correspond to median values within Voronoi cells containing similar numbers of stars. The large symbols with error bars illustrate the mean values of these velocities from the Voronoi cells within radial bins and the resulting standard errors of the mean. Here, orange squares (blue diamonds) correspond to the intermediate-age/old (young) stellar population. The green solid and blue dotted lines are the same as in Fig. 10 but now shown over a larger radial extent. The red solid line indicates the measured rotation curve of the combined stellar population, resulting from the *Gaia* eDR3 data (Gaia Collaboration et al. 2021a).

binned the velocities of the individual Voronoi cells in radial direction to study the behaviour of the rotation velocity as a function of the distance to the centre of the galaxy, as well as a function of the stellar population. The large orange squares and blue diamonds in Fig. 12 show the radially binned velocity data from Schmidt et al. (2022) for the intermediate-age/old ($\gtrsim 2$ Gyr) and young (≤ 1 Gyr) stellar populations, respectively. We can see that the binned mean rotation velocities are consistent with the relation for the intermediate-age/old stellar population derived in this work and the rotation curve resulting from the combined stellar population from the *Gaia* eDR3 data. Within ~ 2.5 kpc, the data from Schmidt et al. (2022) are dominated by the slowly rotating parts of the LMC disc. We note that the young population shows a higher mean rotational velocity than the intermediate-age/old population only within the inner ~ 3.5 kpc, whereas v_ϕ of the young stars falls below the relation we derived for the young population. At radii greater than ~ 4 kpc, the rotational velocities of both the young and intermediate-age/old populations show signs of a decrease. This behaviour of the rotation curve is consistent with previous measurements (e.g. Wan et al. 2020; Gaia Collaboration et al. 2021a; Choi et al. 2022) and is partially caused by elliptical orbits (van der Marel & Cioni 2001).

5.2 Internal velocity maps

To visualize the internal velocity field of the central parts of the LMC, we built spatially resolved velocity maps for the young and intermediate-age/old stellar populations. To produce maps in a more familiar way, we show them in a coordinate system with axes aligned with the local RA and Dec. directions. For this, we rotated the v'_x and v'_y components of the velocities back by the angle Θ . We further projected the RA and Dec. coordinates of the stars to a flat plane using a zenithal equidistant projection as defined in van der Marel & Cioni (2001) with our inferred dynamical centre as the centre of the projection. To construct the maps, we spatially binned the kinematic data using the Voronoi tessellation code developed by Cappellari & Copin (2003) as described by Kamann et al. (2016, 2018).

The resulting velocity map of the intermediate-age/old stellar populations is presented in Fig. 13. The map is composed of 255 Voronoi cells in total, which contain approximately 20000 stars each. The arrows represent the median velocity within these cells. As expected, the map shows overall a regular clockwise rotation pattern. The high-velocity vectors evident near the 30 Doradus star-forming region ($x \sim -1.5^\circ$, $y \sim 0.0^\circ$) are most likely an artefact caused by the combination of the following two effects: first, the short time baseline for the PM calculation (~ 12 months) within tile LMC 6.6 results in large associated uncertainties, and second, the high reddening combined with crowding issues caused by the high stellar densities in this region leads to a low number of stars with measured PMs. In the regions of the bar, we can see deviations from circular orbital motions. Stars seem to move on elongated orbits aligned with the major axis of the stellar bar (see also Fig. A1 for a stream plot representation of the orbits). To quantify this, we calculated for each Voronoi cell the radial component v_r of the normalized median velocity. The resulting map is presented in Fig. 14. The figure shows an increase of v_r within the bar structure, compared to the outer parts, validating the non-circular nature of the orbits in these regions. Such elongated orbits belong to the so-called x_1 family of periodic orbits (see e.g. Contopoulos & Papayannopoulos 1980; Athanassoula et al. 1983; Skokos, Patsis & Athanassoula 2002) and are considered to provide the main contribution for the support of the bar structure. Our velocity map provides the first direct observational evidence for the existence of such orbits within the LMC. It also indicates that the x_1 orbit family indeed is the prevailing one within the bar. This discovery provides an important contribution to the study of dynamical properties of barred galaxies, since the Magellanic Clouds are at present the only galaxies where such orbits can be investigated using PMs (this is not yet possible for galaxies outside the Local Group). The very central parts of the bar close to the dynamical centre show contributions from irregular and chaotic motions (see Fig. 15 for a zoom-in figure of the central region with a finer Voronoi tessellation). Such chaotic velocity structure might be responsible for a homogeneous chemical pattern within the bar by levelling off any metallicity gradient of the various stellar populations inside the bar (see e.g. Choudhury et al. 2021; Grady, Belokurov & Evans 2021).

Fig. 16 shows the map of the velocity field from the young stellar populations. To account for the low number of young stars, this map is composed of 94 Voronoi bins with each cell containing about 3000 stars. The map shows a less ordered velocity structure with a clear regular rotational pattern only evident in the northern and south-western parts. As for the intermediate-age/old stellar population, the motions within the 30 Doradus region are not reliable. The underlying stellar density map in Fig. 16 shows a clear thin, filamentary bar structure of young stars that was already observed in the morphology maps presented by El Youssoufi et al. (2019b). We also note that this structure is offset from the inferred dynamical centre. Within the bar structure, the stars show more irregular motions; however, there seem to be preferred directions of motion that are along the filament.

6 SUMMARY AND CONCLUSIONS

In this study, we applied our techniques to measure stellar PMs to 18 VMC tiles covering ~ 28 deg² of the central regions of the LMC. We derived stellar positions from individual-epoch PSF photometric catalogues spanning time baselines between 12 and 47 months, and calculated absolute PMs with respect to well-measured stars from the *Gaia* eDR3 catalogue. To analyse the resulting PMs, we fitted a simple model of a flat rotating disc to our data. Below we summarize our main results:

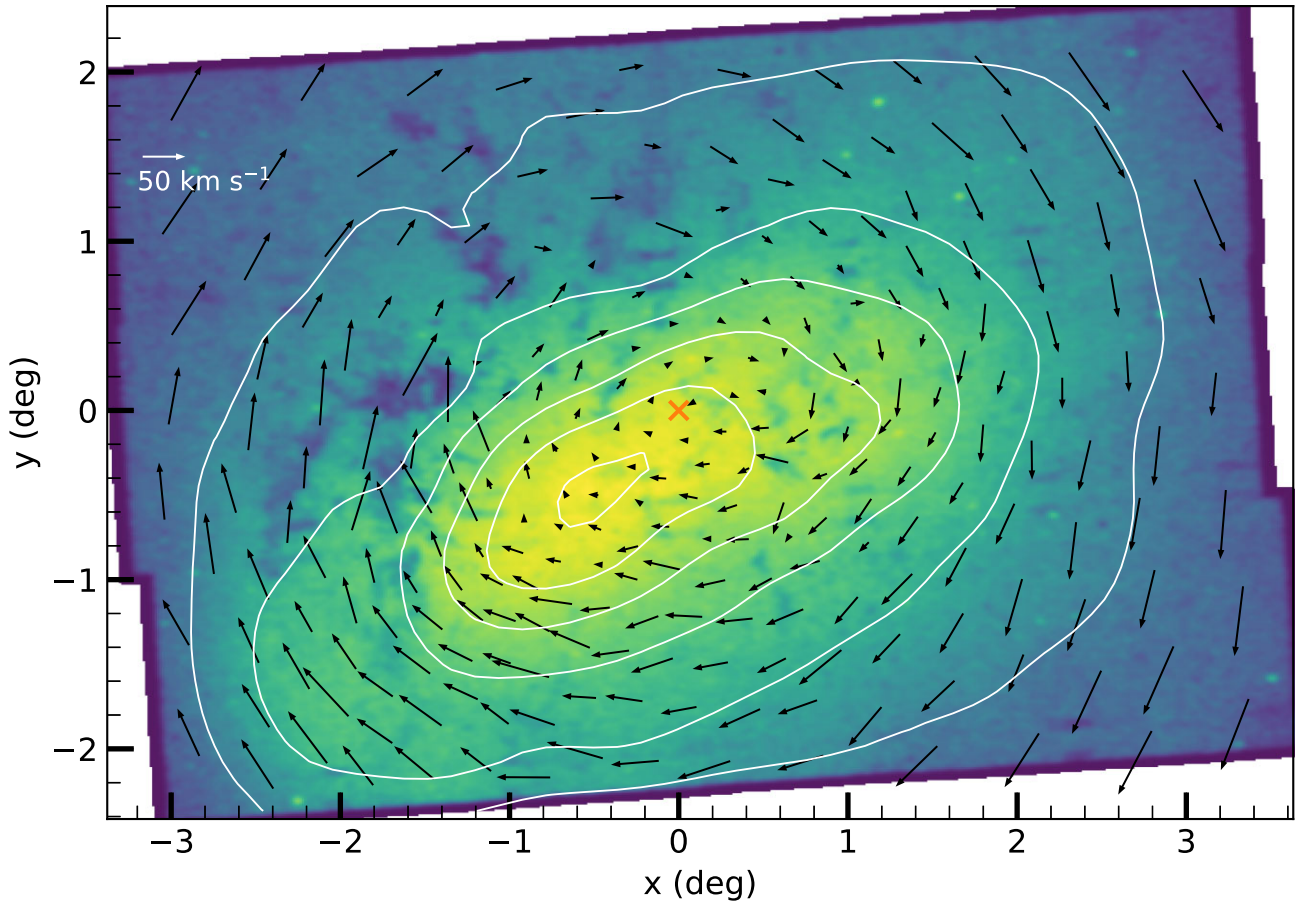


Figure 13. Velocity map of the intermediate-age/old LMC stellar populations. Each arrow represents the median velocity of $\sim 20\,000$ stars. The background colour image illustrates the density of the intermediate-age and old stars with measured VMC PMs. The dynamical centre derived in this study is marked by an orange cross. Also shown as white solid lines are contours of constant stellar density. North is to the top and east is to the left.

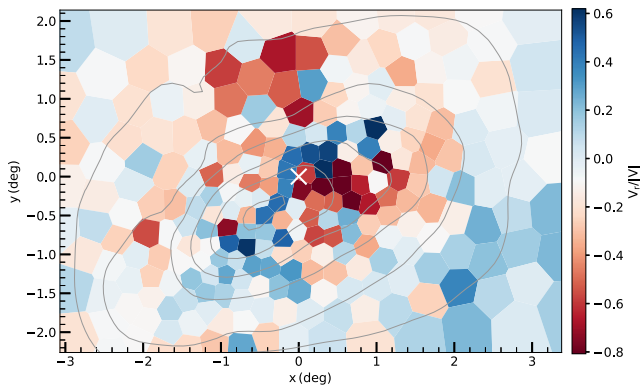


Figure 14. Map of the radial component of the velocities shown in Fig. 13. Each Voronoi cell is colour-coded by the radial component of the normalised velocity vector within each cell. The grey solid lines are the same contours of constant stellar density as in Fig. 13. The dynamical centre is indicated with a white cross.

(i) Leaving the location of the dynamical centre as a free parameter in the fitting, we found coordinates ($\alpha_0 = 79.95^\circ_{-0.23}^{+0.22}$, $\delta_0 = -69.31^\circ_{-0.11}^{+0.12}$). This inferred position of the rotational centre is in close agreement with the one resulting from *HST* measurements (van der Marel & Kallivayalil 2014).

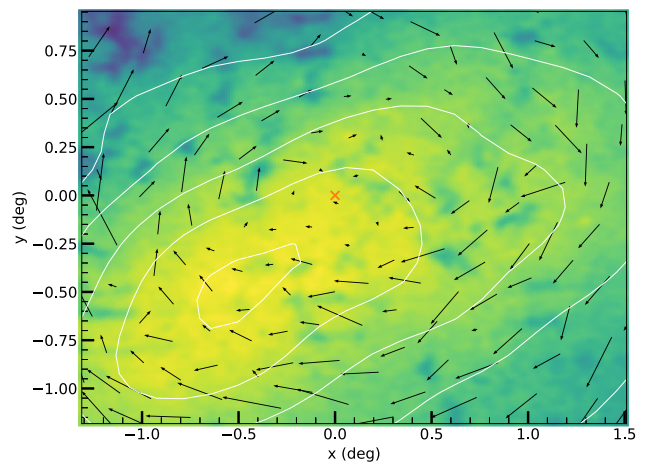


Figure 15. Zoom-in version of Fig. 13 to highlight the velocity field of the bar region. To better visualize the kinematic details, here each arrow represents the median velocity of $\sim 15\,000$ stars, resulting in a finer Voronoi tessellation (346 cells in total).

(ii) We found the orientation angles of the central regions of the LMC (bar and inner disc) to be in general agreement with values from the literature. The inferred value for the inclination ($i = 33.5^\circ_{-1.3}^{+1.2}$) favours a higher inclination of the bar region with respect to the outer

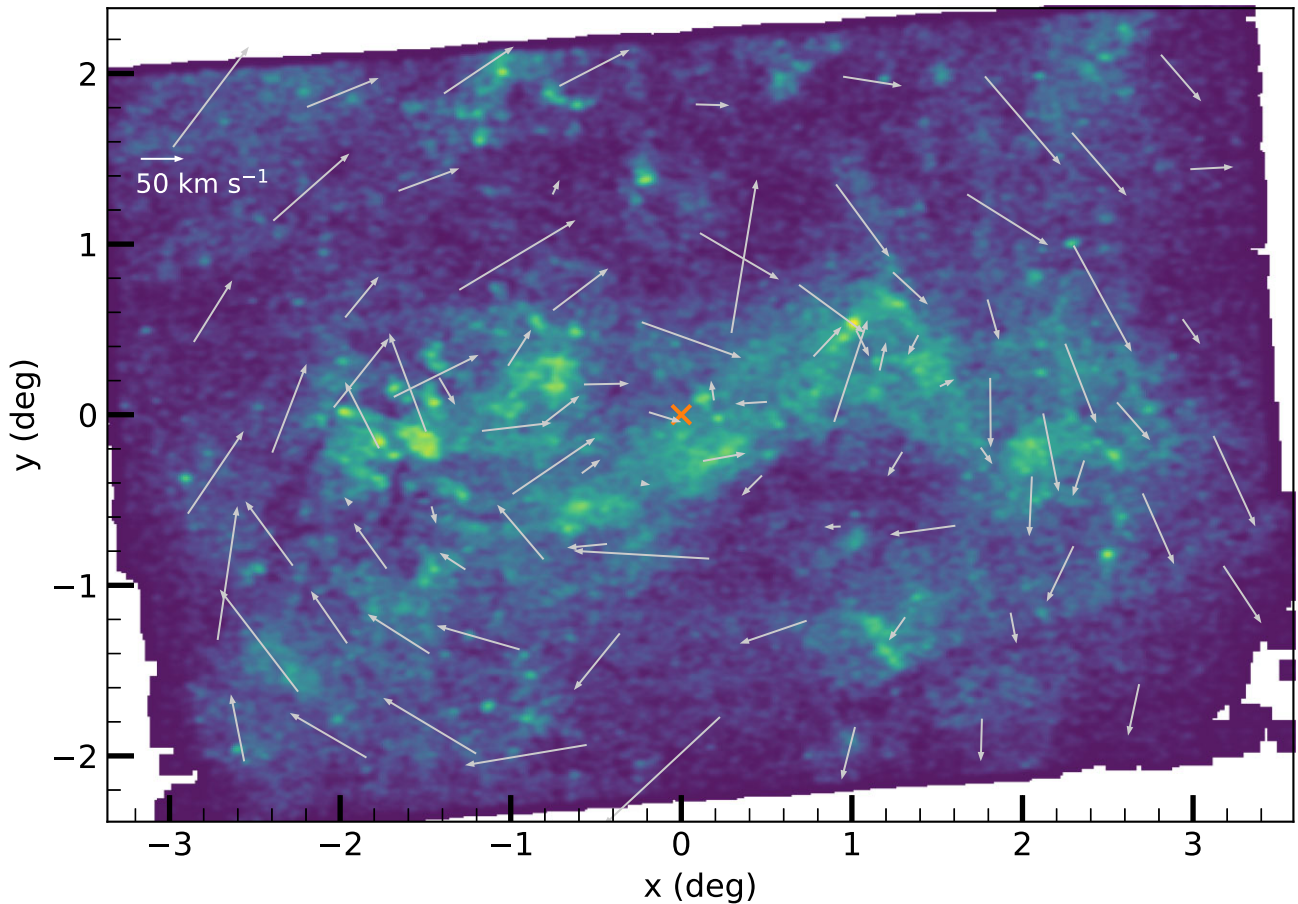


Figure 16. Similar to Fig. 13, but now for the young stellar population. Here, the arrows represent the median velocity of ~ 3000 stars. The background colour image shows the density of young stars with measured VMC PMs.

parts of the disc. Our obtained value for the position angle of the line of nodes ($\Theta = 129.8^{\circ}_{-1.9}^{+1.9}$), meanwhile, is lower than most of the values from other literature studies and is not consistent with the bar having a larger position angle.

(iii) The young stellar population follows a different rotation curve than the intermediate-age/old population with a higher constant rotational velocity, confirming previous findings from PM and radial velocity data. The rotation curve of the AGB stars shows a jump to higher tangential velocity values, which could be explained by AGB stars tracing different morphological features with diverse mean stellar ages.

(iv) Our velocity maps show that intermediate-age/old stars follow elongated orbits that are aligned with the major axis of the bar structure, providing first direct observational evidence for orbits of the x_1 family within the LMC. In the central parts of the bar, the velocity structure of the intermediate-age/old stellar population shows contributions from chaotic motions.

(v) The velocity map of the young stars shows ordered circular motions only in the outer regions of our studied area. In the inner regions, the stars seem to predominantly move along a thin filamentary bar structure composed of young stars that is offset from the inferred dynamical centre.

For future studies, we plan to add one additional epoch of observations in the K_s filter to the original VMC survey. The additional epoch will increase the time baseline for PM calculations from ~ 2 yr to up to 12 yr, which will significantly reduce the

systematic uncertainties of the PM measurements. A combination of these updated PM measurements with large-scale spectroscopic data sets, like the 4MOST One Thousand and One Magellanic Fields (1001MC) survey (Cioni et al. 2019) will provide the unique opportunity to study the chemo-dynamical history of the Magellanic Cloud system in unprecedented detail.

ACKNOWLEDGEMENTS

We thank the Cambridge Astronomy Survey Unit (CASU) and the Wide Field Astronomy Unit (WFAU) in Edinburgh for providing calibrated data products under the support of the Science and Technology Facility Council (STFC). This project has received funding from the European Research Council (ERC) under European Union's Horizon 2020 research and innovation programme (project INTERCLOUDS, grant agreement no. 682115). This research was supported in part by the Australian Research Council Centre of Excellence for All Sky Astrophysics in 3 Dimensions (ASTRO 3D), through project number CE170100013. SS acknowledges support from the Science and Engineering Research Board, India through a Ramanujan Fellowship. This study is based on observations obtained with VISTA at the Paranal Observatory under programme ID 179.B-2003. This work has used data from the European Space Agency (ESA) mission *Gaia* (<https://www.cosmos.esa.int/gaia>), processed by the *Gaia* Data Processing and Analysis Consortium (DPAC, <https://www.cosmos.esa.int/web/gaia/dpac/consortium>). Funding for the DPAC has been provided by national institutions, in

particular the institutions participating in the *Gaia* Multilateral Agreement. We thank Paul McMillan for insightful discussions regarding the modelling of the LMC. We thank Stefano Rubele for the production of the deep tile PSF catalogues and acknowledge the ERC Consolidator Grant funding scheme (project STARKEY, grant agreement 615604) for supporting S. Rubele's work. This research made use of *ASTROPY*,⁷ a community-developed core *PYTHON* package for Astronomy (Astropy Collaboration et al. 2013, 2018), *IPHYTHON* (Perez & Granger 2007), *MATPLOTLIB* (Hunter 2007), *NUMPY* (Harris et al. 2020), and *SCIPY* (Virtanen et al. 2020). We thank the anonymous referee for useful comments and suggestions that helped to improve the paper.

DATA AVAILABILITY

The raw VMC data are publicly available at the ESO archive (http://archive.eso.org/eso/eso_archive_main.html). The calibrated images of the LMC as well as the PSF catalogues of the LMC tiles used in this work to derive the stellar PMs are still proprietary to the VMC team. These data are planned to be released as part of data release 6 of the VMC survey in mid 2022. The PM catalogues will be shared on reasonable request to the corresponding author.

REFERENCES

Astropy Collaboration et al., 2013, *A&A*, 558, A33
 Astropy Collaboration et al., 2018, *AJ*, 156, 123
 Athanassoula E., Bienayme O., Martinet L., Pfenniger D., 1983, *A&A*, 127, 349
 Bell C. P. M. et al., 2019, *MNRAS*, 489, 3200
 Belokurov V. A., Erkal D., 2019, *MNRAS*, 482, L9
 Belokurov V., Erkal D., Deason A. J., Koposov S. E., De Angeli F., Evans D. W., Fraternali F., Mackey D., 2017, *MNRAS*, 466, 4711
 Besla G., Hernquist L., Loeb A., 2013, *MNRAS*, 428, 2342
 Besla G., Kallivayalil N., Hernquist L., van der Marel R. P., Cox T. J., Kereš D., 2012, *MNRAS*, 421, 2109
 Boyce H., Lützgendorf N., van der Marel R. P., Baumgardt H., Kissler-Patig M., Neumayer N., de Zeeuw P. T., 2017, *ApJ*, 846, 14
 Cappellari M., Copin Y., 2003, *MNRAS*, 342, 345
 Choi Y. et al., 2018, *ApJ*, 866, 90
 Choi Y., Olsen K. A. G., Besla G., van der Marel R. P., Zivick P., Kallivayalil N., Nidever D. L., 2022, *ApJ*, 927, 153
 Choudhury S. et al., 2021, *MNRAS*, 507, 4752
 Cioni M.-R. L. et al., 2011, *A&A*, 527, A116
 Cioni M.-R. L. et al., 2014, *A&A*, 562, A32
 Cioni M.-R. L. et al., 2016, *A&A*, 586, A77
 Cioni M. R. L. et al., 2019, *Messenger*, 175, 54
 Conroy C., Naidu R. P., Garavito-Camargo N., Besla G., Zaritsky D., Bonaca A., Johnson B. D., 2021, *Nature*, 592, 534
 Contopoulos G., Papayannopoulos T., 1980, *A&A*, 92, 33
 Cross N. J. G. et al., 2012, *A&A*, 548, A119
 Cullinane L. R., Mackey A. D., Da Costa G. S., Erkal D., Koposov S. E., Belokurov V., 2022, *MNRAS*, 510, 445
 Cusano F. et al., 2021, *MNRAS*, 504, 1
 D'Onghia E., Fox A. J., 2016, *ARA&A*, 54, 363
 Dalton G. B. et al., 2006, in McLean I. S., Iye M., eds, Proc. SPIE Conf. Ser. Vol. 6269, Ground-based and Airborne Instrumentation for Astronomy. SPIE, Bellingham, p. 62690X
 de Grijs R., Bono G., 2015, *AJ*, 149, 179
 de Grijs R., Wicker J. E., Bono G., 2014, *AJ*, 147, 122
 de Vaucouleurs G., Freeman K. C., 1972, *Vistas Astron.*, 14, 163
 Diaz J. D., Bekki K., 2012, *ApJ*, 750, 36

El Youssoufi D. E., Cioni M.-R. L., Bell C. P. M., Rubele S., Niederhofer F., Matijevic G., 2019a, in McQuinn K. B. W., Stierwalt S., eds, Proc. IAU Symp. Vol. 344, Dwarf Galaxies: From the Deep Universe to the Present. Kluwer, Dordrecht, p. 66
 El Youssoufi D. et al., 2019b, *MNRAS*, 490, 1076
 El Youssoufi D. et al., 2021, *MNRAS*, 505, 2020
 Emerson J., McPherson A., Sutherland W., 2006, *Messenger*, 126, 41
 Foreman-Mackey D., 2016, *J. Open Source Softw.*, 24
 Foreman-Mackey D., Hogg D. W., Lang D., Goodman J., 2013, *PASP*, 125, 306
 Gaia Collaboration et al., 2018, *A&A*, 616, A12
 Gaia Collaboration et al., 2021a, *A&A*, 649, A7
 Gaia Collaboration et al., 2021b, *A&A*, 649, A1
 González-Fernández C. et al., 2018, *MNRAS*, 474, 5459
 Goodman J., Weare J., 2010, *Commun. Appl. Math. Computat. Sci.*, 5, 65
 Grady J., Belokurov V., Evans N. W., 2021, *ApJ*, 909, 150
 Hammer F., Yang Y. B., Flores H., Puech M., Fouquet S., 2015, *ApJ*, 813, 110
 Harris C. R. et al., 2020, *Nature*, 585, 357
 Hindman J. V., Kerr F. J., McGee R. X., 1963, *Aust. J. Phys.*, 16, 570
 Hunter J. D., 2007, *Comput. Sci. Eng.*, 9, 90
 Inno L. et al., 2016, *ApJ*, 832, 176
 Irwin M. J. et al., 2004, in Quinn P. J., Bridger A., eds, Proc. SPIE Conf. Ser. Vol. 5493, Optimizing Scientific Return for Astronomy through Information Technologies. SPIE, Bellingham, p. 411
 Irwin M. J., Kunkel W. E., Demers S., 1985, *Nature*, 318, 160
 Jacyszyn-Dobrzyniecka A. M. et al., 2020, *ApJ*, 889, 26
 Kallivayalil N., van der Marel R. P., Alcock C., 2006b, *ApJ*, 652, 1213
 Kallivayalil N., van der Marel R. P., Alcock C., Axelrod T., Cook K. H., Drake A. J., Geha M., 2006a, *ApJ*, 638, 772
 Kallivayalil N., van der Marel R. P., Besla G., Anderson J., Alcock C., 2013, *ApJ*, 764, 161
 Kamann S. et al., 2016, *A&A*, 588, A149
 Kamann S. et al., 2018, *MNRAS*, 473, 5591
 Kim S., Staveley-Smith L., Dopita M. A., Freeman K. C., Sault R. J., Kesteven M. J., McConnell D., 1998, *ApJ*, 503, 674
 Kinson D. A., Oliveira J. M., van Loon J. T., 2021, *MNRAS*, 507, 5106
 Luks T., Rohlf K., 1992, *A&A*, 263, 41
 Mackey A. D., Koposov S. E., Erkal D., Belokurov V., Da Costa G. S., Gómez F. A., 2016, *MNRAS*, 459, 239
 Mackey D., Koposov S., Da Costa G., Belokurov V., Erkal D., Kuzma P., 2018, *ApJ*, 858, L21
 Mathewson D. S., Cleary M. N., Murray J. D., 1974, *ApJ*, 190, 291
 Nidever D. L., Majewski S. R., Butler Burton W., 2008, *ApJ*, 679, 432
 Niederhofer F. et al., 2018a, *A&A*, 612, A115
 Niederhofer F. et al., 2018b, *A&A*, 613, L8
 Niederhofer F. et al., 2021, *MNRAS*, 502, 2859
 Nikolaev S., Drake A. J., Keller S. C., Cook K. H., Dalal N., Griest K., Welch D. L., Kanbur S. M., 2004, *ApJ*, 601, 260
 Nikolaev S., Weinberg M. D., 2000, *ApJ*, 542, 804
 Olsen K. A. G., Massey P., 2007, *ApJ*, 656, L61
 Olsen K. A. G., Zaritsky D., Blum R. D., Boyer M. L., Gordon K. D., 2011, *ApJ*, 737, 29
 Patel E., Besla G., Sohn S. T., 2017, *MNRAS*, 464, 3825
 Pennock C. M. et al., 2021, *MNRAS*, 506, 3540
 Perez F., Granger B. E., 2007, *Comput. Sci. Eng.*, 9, 21
 Richter P., Fox A. J., Wakker B. P., Lehner N., Howk J. C., Bland-Hawthorn J., Ben Bekhti N., Fechner C., 2013, *ApJ*, 772, 111
 Rubele S. et al., 2015, *MNRAS*, 449, 639
 Schmidt T. et al., 2020, *A&A*, 641, A134
 Schmidt T. et al., 2022, preprint ([arXiv:2201.10018](https://arxiv.org/abs/2201.10018))
 Skokos C., Patsis P. A., Athanassoula E., 2002, *MNRAS*, 333, 847
 Skowron D. M. et al., 2021, *ApJS*, 252, 23
 Smith L. C. et al., 2018, *MNRAS*, 474, 1826
 Stetson P. B., 1987, *PASP*, 99, 191
 Subramanian S., Subramaniam A., 2013, *A&A*, 552, A144
 Sutherland W. et al., 2015, *A&A*, 575, A25

⁷<http://www.astropy.org>

- Tody D., 1986, in Crawford D. L., ed., Proc. SPIE Conf. Ser. Vol. 627, Instrumentation in Astronomy VI. SPIE, Bellingham, p. 733
- Tody D., 1993, in Hanisch R. J., Brissenden R. J. V., Barnes J., eds, ASP Conf. Ser. Vol. 52, Astronomical Data Analysis Software and Systems II. Astron. Soc. Pac., San Francisco, p. 173
- van der Marel R. P., 2001, *AJ*, 122, 1827
- van der Marel R. P., Alves D. R., Hardy E., Suntzeff N. B., 2002, *AJ*, 124, 2639
- van der Marel R. P., Cioni M.-R. L., 2001, *AJ*, 122, 1807
- van der Marel R. P., Kallivayalil N., 2014, *ApJ*, 781, 121
- van der Marel R. P., Kallivayalil N., Besla G., 2009, in Van Loon J. T., Oliveira J. M., eds, Proc. IAU Symp. 256, The Magellanic System: Stars, Gas and Galaxies. Cambridge Univ. Press, Cambridge, p. 81
- van der Marel R. P., Sahlmann J., 2016, *ApJ*, 832, L23
- Vasiliev E., 2018, *MNRAS*, 481, L100
- Virtanen P. et al., 2020, *Nature Meth.*, 17, 261
- Wan Z., Guglielmo M., Lewis G. F., Mackey D., Ibata R. A., 2020, *MNRAS*, 492, 782

- Wang J., Hammer F., Yang Y., Ripepi V., Cioni M.-R. L., Puech M., Flores H., 2019, *MNRAS*, 486, 5907
- Wolf C. et al., 2018, *PASA*, 35, e010
- Zhao H., Evans N. W., 2000, *ApJ*, 545, L35
- Zivick P. et al., 2018, *ApJ*, 864, 55
- Zivick P. et al., 2019, *ApJ*, 874, 78

APPENDIX: STREAM PLOT

Fig. A1 shows a velocity stream plot of the intermediate-age/old stellar population to illustrate the elliptical nature of the predominant bar orbits. The streamlines have been created from the median velocity vectors of the stars within a regular 30×30 grid. Also shown as white dashed lines are circular paths for a better comparison of the observed orbits with circular motions.

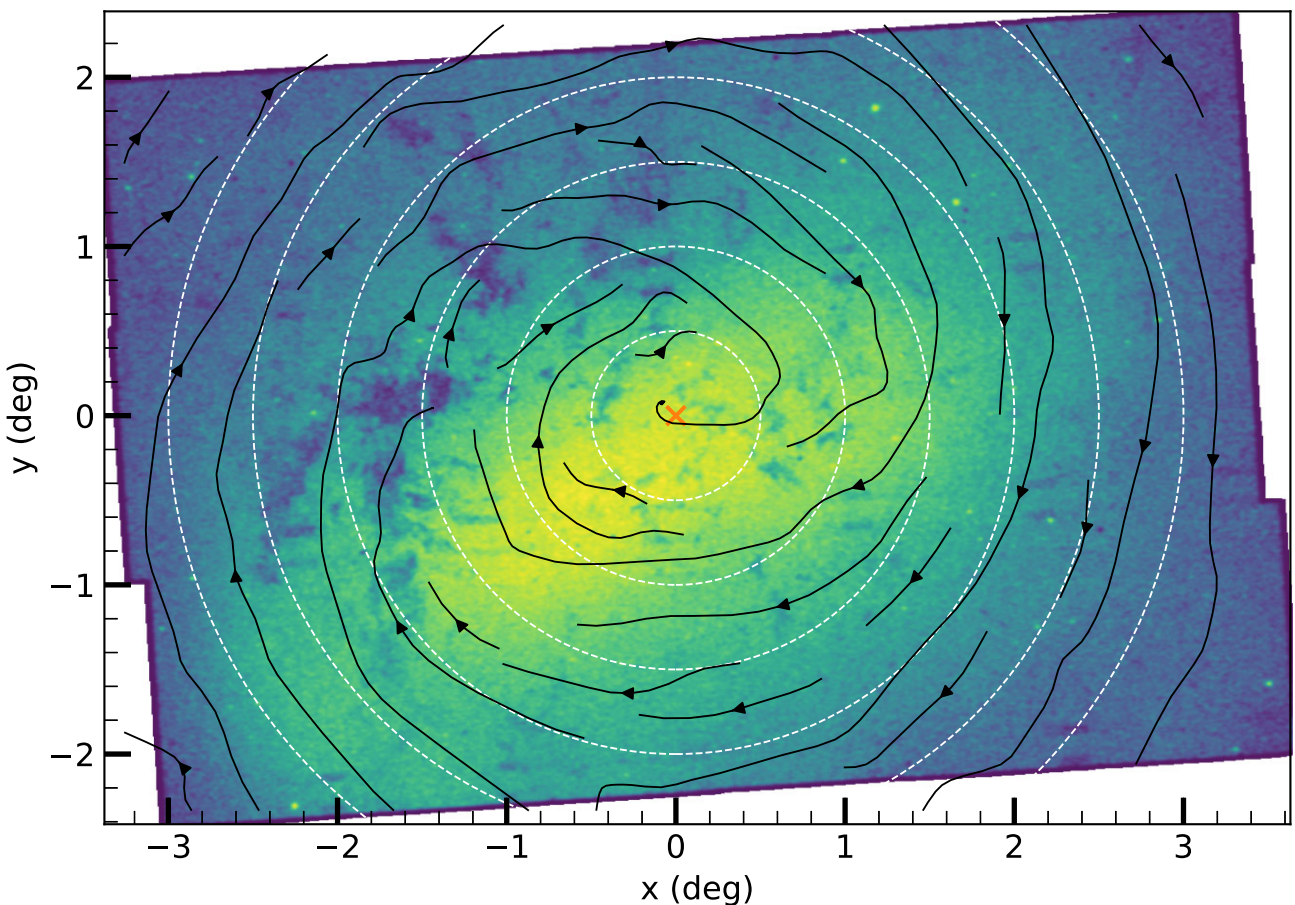


Figure A1. Similar to Fig. 13, but showing velocity streamlines (black solid lines with arrow heads) to better illustrate the elliptical nature of the bar orbits. For comparison, the dashed white curves follow the shapes of circular orbits.

This paper has been typeset from a $\text{\TeX}/\text{\LaTeX}$ file prepared by the author.